Progress in Turbulence Modeling
for Complex Flow Fields Including
Effects of Compressibility

David C. Wilcox and Morris W. Rubesin

APRIL 1980

NASA

NASA Technical Paper 1517

Progress in Turbulence Modeling for Complex Flow Fields Including Effects of Compressibility

David C. Wilcox
DCW Industries, Inc.
Studio City, California

Morris W. Rubesin
Ames Research Center
Moffett Field, California

NASA

National Aeronautics
and Space Administration

**Scientific and Technical
Information Office**

1980

SYMBOLS

C_f local skin-friction coefficient

e turbulent mixing energy (two-equation model)

f ratio of rates of strain in distorted homogeneous flows (eq. (53))

h mass-averaged static enthalpy

h'' mass-averaged fluctuating static enthalpy

K distortion parameter (eq. (63))

k^+ surface roughness parameter, $\dfrac{ku_\tau}{\nu}$

ℓ length scale (eq. (15))

p mean pressure

p' fluctuating pressure

P_e production term in turbulence kinetic energy equation (eq. (1))

q_j mass-averaged turbulent heat-flux vector (eqs. (9))

$q_j{}^T$ mass-averaged total heat flux vector, molecular plus turbulent mechanisms (eq. (7))

R_e scaling Reynolds number for λ^* (eqs. (16) or (39))

R_ω scaling Reynolds number for γ (eqs. (16) or (39))

Re_T turbulence Reynolds number (eq. (17))

S_{ij} mean rate of strain tensor (eq. (8))

$\bar{S}$ absolute magnitude of mean rate of strain, $\sqrt{\overline{S_{ij}S_{ij}}}$

t time

u_i mass-averaged velocity vector

u_i'' mass-averaged fluctuating velocity vector

u_τ friction velocity, $\sqrt{\dfrac{\tau_w}{\rho_w}}$

x_i space coordinate vector, $i = 1, 2,$ or 3

v_w surface blowing rate

v_w^+ normalized surface blowing rate, $\dfrac{v_w}{u_\tau}$

α^* closure coefficient in Saffman's turbulence kinetic energy equation

β closure coefficient in dissipation terms of pseudovorticity or specific dissipation rate equation (eq. (14) or (37))

β^* closure coefficient in turbulent mixing-energy equation (eq. (13))

β^{**} closure coefficient in decay term of heat-flux equation (eq. (36))

γ closure coefficient in production term of specific dissipation rate equation (eq. (14) or (37))

γ^* closure coefficient in eddy diffusivity expression (eq. (12))

δ_{ij} Kronecker delta

ϵ eddy diffusivity

$\bar{\epsilon}$ axial rate of strain in homogeneous flow

ι turbulence kinetic energy ratio factor at boundary-layer edge, $\dfrac{e_e}{u_e^2}$

κ Karman constant

$\bar{\kappa}$ rate of shearing strain in homogeneous flow

λ low turbulent Reynolds number factor for closure coefficient in Reynolds stress redistribution term (eqs. (16) or (39))

λ^* closure coefficient in redistribution term of Reynolds-stress equation (eq. (35))

μ molecular viscosity

ν kinematic viscosity

ρ mean density

$\tilde{\rho}$ ins.antaneous density

σ inverse of the effective Prandtl number for the turbulent diffusion of specific dissipation rate

σ^* inverse of the effective Prandtl number for the turbulent diffusion of Reynolds stress or kinetic energy

σ^{**} inverse of the effective Prandtl number for the turbulent diffusion of heat flux

τ_{ij} mass averaged specific Reynolds stress tensor (eqs. (9))

τ_{ij}^T mass averaged specific total stress tensor, molecular plus turbulent transport (eq. (6))

ϕ_{ij} correlation of pressure and rate of strain fluctuations

χ damping coefficient for ν^*

Ω_{ij} mean vorticity tensor

ω pseudovorticity or specific dissipation rate

Subscripts

w   surface value

o   initial value

e   boundary-layer edge value

Superscripts

+   "law of the wall" coordinate

$$u^+ = \frac{u}{u_\tau} \ , \quad y^+ = y \, \frac{u_\tau}{\nu_w}$$

PROGRESS IN TURBULENCE MODELING FOR COMPLEX FLOW FIELDS

INCLUDING EFFECTS OF COMPRESSIBILITY

David C. Wilcox[*] and Morris W. Rubesin[†]

SUMMARY

Two second-order-closure turbulence models have been devised that are suitable for predicting properties of complex turbulent flow fields in both incompressible and compressible fluids. One model is of the "two-equation" variety in which closure is accomplished by introducing an eddy viscosity which depends on both a turbulent mixing energy and a dissipation rate per unit energy, that is, a *specific* dissipation rate. The other model is a "Reynolds stress equation" (RSE) formulation in which all components of the Reynolds stress tensor and turbulent heat-flux vector are computed directly and are scaled by the specific dissipation rate. Computations based on these models are compared with measurements for the following flow fields: (a) low speed, high Reynolds number channel flows with plane strain or uniform shear; (b) equilibrium turbulent boundary layers with and without pressure gradients or effects of compressibility; and (c) flow over a convex surface with and without a pressure gradient. The RSE model-computed flow properties generally differ by less than 10% from the measurements for all of the applications. Discrepancies between two-equation model predictions and the measured flow properties are much larger only for homogeneous flows with suddenly applied strain, lending further credence to the notion that a Reynolds stress model offers little advantage over a two-equation model for two-dimensional boundary layers that are close to equilibrium.

INTRODUCTION

For the past several years, Wilcox and his colleagues have made significant progress in developing second-order closure models suitable for computing complex turbulent flows, including the effects of compressibility (refs. 1 and 2). While early emphasis was focused on two-dimensional attached flows with curved streamlines, care was taken to ensure that, at least in principle, the models could be applied in a straightforward way to both separated and three-dimensional flows. Although most of the modeling effort was devoted to the development of a "two-equation" eddy viscosity model of turbulence, this work was guided to some extent by the parallel development of a model for the Reynolds stress tensor equation. These models were significant improvements of the two-equation model originally devised by Saffman (ref. 3) and Wilcox (refs. 4 to 6). Most importantly, the model presented by Wilcox and Traci

[*]President, DCW Industries, Inc., Studio City, CA 91604
[†]Sr. Staff Scientist, Ames Research Center, NASA, Moffett Field, CA 94035

(ref. 6) is as accurate as mixing length theory for equilibrium boundary layers[1] and has a much wider range of applicability, for example, reference 7.

Throughout the development of these models, the production terms for the turbulence kinetic energy were maintained as in Saffman's original work (ref. 3) where the production of turbulence kinetic energy was set proportional to the kinetic energy times the absolute value of the rate of strain. Although this approach led to a mathematically elegant homogeneous equation for the turbulence kinetic energy, it introduced modeling for terms that can be derived directly. For attached boundary layers, Saffman's additional modeling introduced no significant differences. When more general flow fields were considered, the Saffman-type production terms were demonstrated to contain the potential for introducing errors. For example, if the homogeneous turbulence field along the centerline of an expanding supersonic nozzle is considered, the actual production of kinetic energy is given by

$$P_e = -\overline{(\widetilde{\rho u_i'' u_j''})} \frac{\partial u_i}{\partial x_j} \tag{1}$$

For this flow field, only *normal* stresses exist, and thus the stresses that appear in equation (1) are positive. As the corresponding rates of strain are also positive, equation (1) then indicates a decrease in the kinetic energy along the centerline of the nozzle. For this same flow field, the Saffman production term

$$P_e = \alpha^* \rho \bar{S} e \tag{2}$$

indicates an *increase* in kinetic energy since the kinetic energy e and the absolute magnitude of the rate of strain tensor $\bar{S}$ are both positive. The rather gross discrepancy for this example (and for others as well) suggested revision of the production terms in the Wilcox-Traci model. Thus, one objective of the current work was to reintroduce the unmodeled production terms into the model equation for the kinetic energy.

During the development of the Wilcox-Traci model, several advances in turbulence modeling were introduced that are not common, as a group, to most of the models found in the literature. First, the effects of compressibility have been accounted for through the use of mass-weighted averaged dependent variables and some hypotheses regarding terms in which the compressibility effects are isolated. Second, several modeling coefficients have been made to depend on the turbulence Reynolds number and this, together with the introduction of molecular diffusivity as a parallel transport mechanism to the turbulence, has permitted integration of the transport and modeling equations directly to surfaces bordering the flow fields. Thus, the relatively common use of a "law of the wall" to define the boundary conditions near surfaces was avoided. Finally, a Reynolds stress tensor model for compressible and low

---

[1]A boundary layer is defined as being in equilibrium if its local skin friction, momentum and displacement thicknesses are consistent with the Ludweig-Tillman formula (ref. 8).

2

Reynolds number flows was developed in parallel with the two-equation model to guide the development and assess the limitations of the latter. A second objective of this paper, then, is to modify the production terms in the Reynolds stress tensor model and to compare the results of computations based on this model with computations from the two-equation model for a series of homogeneous and boundary-layer flows that are well documented with measurements of the turbulence quantities.

FORMULATION OF MODEL EQUATIONS

Mean Flow Equations and Boundary Conditions

For a compressible fluid in turbulent flow, the conservation equations for mass, momentum, and energy are written in terms of the mass-weighted average quantities as follows:

$$\frac{\partial \rho}{\partial t} + \frac{\partial}{\partial x_i} (\rho u_i) = 0 \tag{3}$$

$$\frac{\partial}{\partial t} (\rho u_i) + \frac{\partial}{\partial x_j} (\rho u_j u_i) = -\frac{\partial p}{\partial x_i} + \frac{\partial}{\partial x_j} (\rho \tau_{ij}^T) \tag{4}$$

$$\frac{\partial}{\partial t} (\rho h) + \frac{\partial}{\partial x_j} (\rho u_j h) = \frac{\partial p}{\partial t} + u_j \frac{\partial p}{\partial x_j} + \rho \tau_{ij}^T \frac{\partial u_i}{\partial x_j} - \frac{\partial}{\partial x_j} (\rho q_j^T) \tag{5}$$

Here, the symbols τ_{ij}^T and q_j^T denote the specific mass-weighted average total shear stress and heat flux that include the contributions of both the molecular and turbulent transport. These quantities are defined as

$$\tau_{ij}^T = 2\nu \left(S_{ij} - \frac{1}{3} \frac{\partial u_k}{\partial x_k} \delta_{ij} \right) + \tau_{ij} \tag{6}$$

and

$$q_j^T = \frac{\nu}{Pr_L} \frac{\partial h}{\partial x_j} + q_j \tag{7}$$

These "specific" quantities are the actual total shear stress and heat flux divided by the local mean density. The mean rate of strain tensor appearing in equation (6) is given by

$$S_{ij} = \frac{1}{2} \left(\frac{\partial u_i}{\partial x_j} + \frac{\partial u_j}{\partial x_i} \right) \tag{8}$$

Finally, τ_{ij} and q_j are the mass-weighted averaged Reynolds stress tensor and heat flux vector defined by

$$\tau_{ij} = -\frac{\langle \widetilde{\rho} u_i'' u_j'' \rangle}{\rho} \left.\begin{array}{c} \\ \\ \\ \\ \end{array}\right\}$$

$$q_j = \frac{\langle \widetilde{\rho} u_j'' h'' \rangle}{\rho}$$

$$(9)$$

where $\widetilde{\rho}$ is the instantaneous density, $\langle\ \rangle$ denotes the time average of the enclosed quantity and the superscript $''$ represents the fluctuating part in a mass-weighted average formulation. The boundary conditions for equations (3) to (5) at surfaces $(x_2 = 0)$ are

$$u_1 = 0$$

$$u_2 = 0 \quad \text{or} \quad v_w(x_1) \qquad\qquad (10)$$

$$h = h_w(x_1) \quad \text{or} \quad \frac{\partial h}{\partial x_2} = \left(\frac{\partial h}{\partial x_2}\right)_w$$

All flow variables approach free-stream flow conditions in general flow field computations. For the special case of two-dimensional boundary layers, the boundary conditions at the boundary-layer edge are at $x_2 = \delta(x_1)$

$$u_1 = U_e(x_1) \left.\begin{array}{c} \\ \\ \end{array}\right\}$$

$$h = h_e(x_1) \qquad\qquad (11)$$

In this section, two models are developed for evaluating the τ_{ij} and q_j defined by equations (9). The first is of the "two-equation" type employing an eddy diffusivity that depends algebraically on the dependent variables of the two modeling equations. This model is a direct extension of the model of reference 6 through the use of unmodeled production terms and a constitutive relationship that permits nonaligned stress and strain. As with all eddy diffusivity models, sudden changes in the rates of strain result in immediate changes in the Reynolds stresses and heat fluxes, although the eddy diffusivity itself has not had time to respond. To remedy this situation, Saffman (ref. 9) developed a method for a two-equation model that permits stress and strain to develop at different rates. Although this method showed promise, it complicated the modeling process by introducing an additional lag equation. The authors felt that the use of Reynolds stress modeling equations could achieve these same objectives regarding the relaxation of equilibrium between stress and strain in a more direct fashion. The Reynolds stress approach eliminated the need for an assumed form of constitutive relationship between stress and strain. Further it was felt that an understanding of the rates of interaction between the individual Reynolds stresses, not forced by a constitutive relationship, would lead to a more general model for three-dimensional flows and, perhaps, ould provide guidance for improving the form of the simpler model and defin. the flow conditions for its validity.

4

Two-Equation Model

The two-equation eddy diffusivity model proposed herein is a direct extension of the Wilcox-Traci model of reference 6. The differences occur within the production terms of the kinetic energy and specific dissipation rate equations[2] and in the constitutive relationship between the Reynolds stresses and the mean rates of strain and vorticity. For the reasons cited in the Introduction, the production term in the kinetic energy equation is retained as the sum of the products of the local Reynolds stress times the appropriate mean velocity gradient, equation (1). The analogous term of the specific dissipation rate equation expressed in ω^2 is modeled as the product of the production term of the kinetic energy equation, the ratio ω^2/e and a new modeling coefficient. This approach is in keeping with the customary way of arriving at the individual terms for the second equation in two-equation models. Other than the production terms and the choice of density scaling for ω, the model equations are virtually identical to those of Wilcox-Traci (ref. 6). The definition of the eddy diffusivity is

$$\epsilon = \gamma^* \frac{e}{\omega} \tag{12}$$

where the turbulence kinetic energy and specific energy dissipation rate are given by the turbulence modeling equations:

$$\frac{\partial}{\partial t} (\rho e) + \frac{\partial}{\partial x_j} (\rho u_j e) = \rho \tau_{ij} \frac{\partial u_i}{\partial x_j} - \beta^* \rho \omega e + \frac{\partial}{\partial x_j} \left[(\mu + \sigma^* \rho \epsilon) \frac{\partial e}{\partial x_j} \right] \tag{13}$$

and

$$\frac{\partial}{\partial t} (\rho \omega^2) + \frac{\partial}{\partial x_j} (\rho u_j \omega^2) = \gamma \frac{\omega^2}{e} \rho \tau_{ij} \frac{\partial u_i}{\partial x_j} - \left[\beta + 2\sigma \left(\frac{\partial \ell}{\partial x_k} \right)^2 \right] \rho \omega^3$$
$$+ \frac{\partial}{\partial x_j} \left[(\mu + \sigma \rho \epsilon) \frac{\partial \omega^2}{\partial x_j} \right] \tag{14}$$

where the length scale is represented by

$$\ell = \frac{e^{1/2}}{\omega} \tag{15}$$

The modeling closure coefficients employed are as follows:

---

[2]These equations differ from what has become the classical two-equation model of turbulence (ref. 10) in that the authors interpret e as a "mixing" energy more akin to $9/4\ \bar{v}'^2$ than to the total turbulence kinetic energy in a boundary layer, and further, feel that ω, the rate of dissipation of kinetic energy *per unit of kinetic energy,* may be a more significant quantity than the rate of turbulence dissipation itself.

$$\beta = \frac{3}{20} \ , \qquad \beta^* = \frac{9}{100} \ , \qquad \sigma = \sigma^* = \frac{1}{2}$$

$$\gamma^* = [1 - (1 - \lambda^2)\exp(-Re_T/R_e)]$$

$$\gamma\gamma^* = \gamma_\infty[1 - (1 - \lambda^2)\exp(-Re_T/R_\omega)] \tag{16}$$

$$\gamma_\infty = \frac{10}{9} \ , \qquad \lambda = \frac{1}{11} \ , \qquad R_e = 1 \ , \qquad R_\omega = 2$$

The Reynolds number of turbulence is given by

$$Re_T = \frac{e^{1/2}\ell}{\nu} \tag{17}$$

The boundary conditions appropriate to these modeling equations when applied to boundary layers have been guided by asymptotic analysis and reference to other models. The surface boundary conditions for equations (13) and (14) are as follows:

At $x_2 = 0$

$$e = 0$$

$$\omega \rightarrow \frac{20\nu_w}{\beta x_2^2} \qquad \text{for smooth impervious wall}$$

or

$$\omega \rightarrow \frac{S}{\sqrt{\beta^*}} \frac{U_\tau^2}{\nu_w} \qquad \text{for a rough and/or porous wall} \tag{18}$$

where

$$S^{-1} = S_R^{-1} + S_B^{-1} \ ; \qquad \text{and} \qquad S_R = \left(\frac{36}{k^+}\right)^2 + \left(\frac{8}{k^+}\right)^{1/2}$$

$$S_B = \frac{6}{v_w^+(1 + v_w^+)}$$

(See ref. 6 for details of the porous or rough wall formulation.)

At $x_2 = \delta$

$$e = \imath U_e^2(x_1)$$

$$\ell = 0.09 \ \beta^{*1/4}\delta(x_1) \tag{19}$$

As discussed in reference 6, the quantity $\ell/\beta^{*1/4}$ behaves much like the classical mixing length. With this understanding, the proportionality coefficient of 0.09 in equations (19) is readily seen to be consistent with the Escudier (ref. 11) eddy-viscosity model for boundary layers.

6

To model Reynolds stresses that do not necessarily align with the mean rates of strain, the constitutive relationship relating these quantities was expanded to

$$\tau_{ij} = -\frac{2}{3}\, e\delta_{ij} + 2\varepsilon\left(S_{ij} - \frac{1}{3}\frac{\partial u_k}{\partial x_k}\,\delta_{ij}\right) + \frac{8}{9}\,\frac{e}{(\beta^*\omega^2 + 2S_{mn}S_{nm})}\,(S_{im}\Omega_{mj} + S_{jm}\Omega_{mi})$$

(20)

where the third term on the right was absent in the Wilcox-Traci model. The vorticity tensor used here is defined as

$$\Omega_{ij} = \frac{1}{2}\left(\frac{\partial u_i}{\partial x_j} - \frac{\partial u_j}{\partial x_i}\right)$$

(21)

The form of equation (20) was guided to some extent by Saffman's constitutive relationship, derived in reference 9, where the Reynolds stress is expressed in a tensor series to quadratic terms in the mean rates of strain and the vorticity

$$\tau_{ij} = -\frac{2}{3}\, e\delta_{ij} + \frac{2Ae}{\omega}\,S_{ij} - \frac{Be}{\omega^2}\,S^2_{k\ell}\delta_{ij} - \frac{Ce}{\omega^2}\,S_{ik}S_{jk}$$

$$- \frac{De}{\omega^2}\,(S_{jk}\Omega_{ik} + S_{ik}\Omega_{jk}) - \frac{Fe}{\omega^2}\,\Omega^2_{k\ell}\delta_{ij} - \frac{Ge}{\omega^2}\,\Omega_{ik}\Omega_{jk}$$

(22)

where A, B, C, D, F, and G are modeling coefficients. Note that equation (22) applies to incompressible flows. In the current work, Saffman's distinction between equilibrium and nonequilibrium kinetic energy is dropped, and this has consequences in the evaluation of the modeling coefficients A through G. The quantity e in equation (22) is identified here with the kinetic energy of the modeling equation (eq. (13)).

Equation (22) can be simplified by requiring it to conform with certain fundamental experimental observations. The experiment of Tucker and Reynolds (ref. 12) where a homogeneous, nearly isotropic turbulence field is distorted by mean normal strains, indicates that under the normal straining

$$u_1 = \bar{\varepsilon}x_1 , \qquad u_2 = -\bar{\varepsilon}x_2 , \qquad \text{and} \qquad u_3 = 0$$

(23)

the normal Reynolds stresses are related approximately as

$$\tau_{33} = \frac{1}{2}\,(\tau_{11} + \tau_{22})$$

(24)

If the conditions represented by equations (23) and (24) are introduced into equation (22), it is found that $C = 0$ is necessary. In addition, in reference 13, it was found that a field of homogeneous turbulence in rigid body rotation decays without developing an isotropy. This observation requires $G = 0$.

If equation (22), with $C = 0$ and $G = 0$, is applied to a shear layer where the only velocity gradient that exists is $\partial u_1/\partial x_2$, it is found that equation (24) again applies and that $B + F = 0$ is required to assure that the magnitude of the trace of the normal Reynolds stresses is equal to twice the kinetic energy. With these values for the coefficients, the Saffman formulation equation (22) reduces to

$$\tau_{ij} = -\frac{2}{3} e \delta_{ij} + \frac{2Ae}{\omega} S_{ij} + \frac{De}{\omega^2} (S_{jk}\Omega_{ki} + S_{ik}\Omega_{kj}) - \frac{Be}{\omega^2} (S_{k\ell}^2 - \Omega_{k\ell}^2)\delta_{ij} \quad (25)$$

It should be noted that in a shear layer or in a boundary layer, the last term of equation (25), containing the factor B, is negligibly small. As the authors' interest is primarily in such shear flows, the term containing B was dropped in the development of equation (20). Equations (25) and (20) differ in other respects. The term $S_{mn}S_{mn}$ that appears in equation (20) was necessary in the computations to avoid sign difficulties at the outer edge of the boundary layers where the values of the normal Reynolds stresses are relatively small. The term $\partial u_k/\partial x_k$ was introduced to account for compressibility and to force the trace of the second term on the right in equation (20) to vanish. The coefficient A was identified with the $\gamma*$ in equation (12). Finally, the quantities $\beta*$ and 8/9 were introduced in the last term to satisfy some boundary-layer needs. These can be seen by writing equation (20) for the logarithmic region of a flat plate boundary layer in incompressible flow. There the only mean velocity gradient of consequence is $\partial u_1/\partial x_2$ so that

$$S_{12} = \frac{1}{2} \frac{\partial u_1}{\partial x_2} , \qquad S_{21} = \frac{1}{2} \frac{\partial u_1}{\partial x_2} \quad (26)$$

with the rest of the components of the rate of strain tensor being orders of magnitude smaller. Similarly, the only components of vorticity of importance are

$$\Omega_{12} = \frac{1}{2} \frac{\partial u_1}{\partial x_2} , \qquad \Omega_{21} = -\frac{1}{2} \frac{\partial u_1}{\partial x_2} \quad (27)$$

With equations (26) and (27), τ_{12} from equation (20) can be written as

$$\tau_{12} = \varepsilon \frac{\partial u_1}{\partial x_2} = \gamma* \frac{e}{\omega} \frac{\partial u_1}{\partial x_2} \quad (28)$$

In this region of the boundary layer, a balance exists between the production and dissipation of turbulence kinetic energy in equation (13), thus

$$\rho\tau_{12} \frac{\partial u_1}{\partial x_2} = \beta*\rho\omega e \quad (29)$$

which leads directly to

$$\beta*\omega^2 = \left(\frac{\partial u_1}{\partial x_2}\right)^2 \quad (30)$$

8

when γ^* is set equal to unity because of the high turbulence Reynolds number in the logarithmic region of the boundary layer (refer to eqs. (16)). The normal components of the Reynolds stress tensor in the logarithmic region become

$$
\left.
\begin{aligned}
\tau_{11} &= -e\left[\frac{2}{3} + \frac{8}{9}\left(\frac{1}{4}\right)\right] = -e\left(\frac{8}{9}\right) \\[2mm]
\tau_{22} &= -e\left[\frac{2}{3} - \frac{8}{9}\left(\frac{1}{4}\right)\right] = -e\left(\frac{4}{9}\right) \\[2mm]
\tau_{33} &= -e\left(\frac{2}{3}\right) \qquad\qquad = -e\left(\frac{6}{9}\right)
\end{aligned}
\right\}
\tag{31}
$$

and are in the ratio

$$
\tau_{11} : \tau_{22} : \tau_{33} = 4:2:3
$$

Also, in this region of a flat plate boundary layer

$$
\tau_{12} \cong \tau_w
\tag{32}
$$

so that equations (29) and (30) combine to indicate

$$
e = \frac{\tau_w/\rho}{\beta^{*1/2}}
\tag{33}
$$

In parallel to these equations, the Reynolds heat flux vectors are represented as

$$
q_j = \frac{\varepsilon}{Pr_T} \frac{\partial \bar{h}}{\partial x} = \frac{\gamma^*}{Pr_T} \frac{e}{\omega} \frac{\partial \bar{h}}{\partial x_j}
\tag{34}
$$

where Pr_T, the turbulent Prandtl number, is usually assigned a value of about 0.9. Comparisons of these modeling conditions with several sets of boundary-layer data are given in later sections of this report.

Reynolds-Stress Model

The Reynolds stress formulation presented herein is a straightforward extension of the model developed in reference 2. For completeness, discussion in this section reviews some of the material presented in reference 2, particularly that pertaining to closure approximations. The key theoretical advantages for using the Reynolds stress model over the usual eddy viscosity model lie in removing the postulates that the principal axis of the Reynolds stress tensor align with that of the mean strain-rate tensor and that sudden changes in the mean strain tensor are reflected immediately in the Reynolds stress. In terms of mass-averaged dependent variables, the Reynolds stress equation or RSE model is expressed in terms of components of Reynolds stress as

$$\frac{\partial}{\partial t}\left(\rho\tau_{ij}\right) + \frac{\partial}{\partial x_k}\left(\rho u_k\tau_{ij}\right) = -\rho\tau_{im}\frac{\partial u_j}{\partial x_m} - \rho\tau_{jm}\frac{\partial u_i}{\partial x_m} + \frac{2}{3}\,\beta^{\star}\rho\omega e\delta_{ij} - \lambda^{\star}\rho\omega$$
$$\times\left(\tau_{ij} + \frac{2}{3}\,e\delta_{ij}\right) + \rho\left(\tau_{jm}S_{mi} + \tau_{im}S_{mj} - \frac{2}{3}\,\tau_{mn}S_{nm}\delta_{ij}\right)$$
$$+ \frac{4}{3}\,\rho e\left(S_{ij} - \frac{1}{3}\frac{\partial u_k}{\partial x_k}\,\delta_{ij}\right) + \frac{\partial}{\partial x_k}\left[(\mu + \sigma^{\star}\rho\varepsilon)\,\frac{\partial\tau_{ij}}{\partial x_k}\right]$$

(35)

The components of the Reynolds heat flux are modeled with

$$\frac{\partial}{\partial t}\left(\rho q_i\right) + \frac{\partial}{\partial x_j}\left(\rho u_j q_i\right) = \rho\tau_{ij}\frac{\partial h}{\partial x_j} - \rho q_j\frac{\partial u_i}{\partial x_j} - \beta^{\star\star}\rho\omega q_i$$
$$+ \frac{\partial}{\partial x_j}\left[\left(\frac{\mu}{Pr_L} + \sigma^{\star\star}\rho\varepsilon\right)\frac{\partial q_i}{\partial x_j}\right]$$

(36)

The specific dissipation rate is given, again, by

$$\frac{\partial}{\partial t}\left(\rho\omega^2\right) + \frac{\partial}{\partial x_j}\left(\rho u_j\omega^2\right) = \gamma\,\frac{\omega^2}{e}\,\rho\tau_{ij}\frac{\partial u_i}{\partial x_j} - \left[\beta + 2\sigma\left(\frac{\partial\ell}{\partial x_k}\right)^2\right]\rho\omega^3$$
$$+ \frac{\partial}{\partial x_j}\left[(\mu + \sigma\rho\varepsilon)\,\frac{\partial\omega^2}{\partial x_j}\right]$$

(37)

where

$$\varepsilon = \frac{e}{\omega}$$
$$e = -\frac{1}{2}\,\tau_{ii}$$
$$\chi = \sqrt{\frac{2S_{mn}S_{nm}}{\beta^{\star}\omega^2}}$$

(38)

The modeling coefficients are:

$$\left.\begin{aligned}
&\beta = \frac{3}{20}\,, \qquad \beta^{\star} = \frac{9}{100}\,, \qquad \beta^{\star\star} = \frac{9}{25}\,, \qquad \sigma = \sigma^{\star} = \frac{1}{2}\,, \qquad \sigma^{\star\star} = 2\\
&\lambda^{\star} = \lambda^{\star}_{\infty}\left[1 - (1 - \lambda^2)\exp(-Re_T/R_e)\right]^{-1}\\
&\frac{\gamma}{\lambda^{\star}} = \frac{\gamma_{\infty}}{\lambda^{\star}_{\infty}}\left[1 - (1 - \lambda^2)\exp(-Re_T/R_\omega)\right]\\
&\lambda^{\star}_{\infty} = \left[\frac{9}{2} - \frac{5}{2}\exp(-5\chi)\right]\beta^{\star}\\
&\gamma_{\infty} = \frac{13}{11}\,, \qquad \lambda = \frac{1}{14}\,, \qquad R_e = 1\,, \qquad R_\omega = 3
\end{aligned}\right\}$$

(39)

Again, the Reynolds number of turbulence, Re_T, is given by equations (15) and (17). At a solid surface, equations (18) again apply and, in addition, at $x_2 = 0$

$$q_j = 0$$
$$\tau_{ij} = 0$$

(40)

At a boundary-layer edge, in addition to equations (19), it is required that at $x_2 = \delta$

$$\left.\begin{array}{l} q_j = 0 \\ \tau_{ij} = \dfrac{2}{3} \iota U_e^2(x_1)\delta_{ij} \end{array}\right\}$$

(41)

where the latter assumes isotropic free-stream tur ulence.

To explain the closure approximations employed, attention is first focused on the heat flux equation (eq. (36)), and the specific dissipation-rate equation (eq. (37)). The first two terms on the right side of equation (36) are the exact heat flux production terms. The next term is the modeled dissipation, while the last term is the modeled turbulent diffusion. It is assumed that the dissipation of the heat flux is proportional to the heat flux vector and that the turbulent diffusion of the heat flux is a simple gradient diffusion process. For the specific dissipation rate equation, the only difference between equation (37) and that used for the two-equation model (eq. (14)), is in the form of the coefficient γ. An explanation of these differences is given in the section entitled "Near Wall Viscous Modifications."

In the Reynolds stress equations, the first two terms on the right-hand side are the exact, unmodeled production terms. The third term is the modeled dissipation. The next three terms model the correlation of the pressure and rate of strain fluctuations. The final term is the sum of the exact molecular diffusion and modeled turbulent diffusion of the Reynolds stress.

It is illuminating to compare those modeled terms with other models. For incompressible flow, the correlation of fluctuations in the pressure and rate strain, Φ_{ij}, namely,

$$\Phi_{ij} = \overline{p'\left(\frac{\partial u_i'}{\partial x_j} + \frac{\partial u_j'}{\partial x_i}\right)}$$

(42)

has been modeled by Launder, Reese, and Rodi (ref. 14) with the rather complete form

$$\Phi_{ij} = C_1\beta^\star\omega\left(\tau_{ij} + \frac{2}{3}\delta_{ij}e\right) - \hat{\alpha}\left(P_{ij} - \frac{2}{3}P\delta_{ij}\right) - \hat{\beta}\left(D_{ij} - \frac{2}{3}P\delta_{ij}\right) - \dot{\gamma}eS_{ij}$$

(43)

where C_1, $\hat{\alpha}$, $\hat{\beta}$, and $\dot{\gamma}$ are the Launder et al. closure coefficients, and

11

$$\left. \begin{array}{l} P_{ij} = \tau_{ik}\dfrac{\partial u_j}{\partial x_k} + \tau_{jk}\dfrac{\partial u_i}{\partial x_k} \\[12pt] D_{ij} = \tau_{ik}\dfrac{\partial u_k}{\partial x_j} + \tau_{jk}\dfrac{\partial u_k}{\partial x_i} \\[12pt] P = \dfrac{1}{2}P_{ii} = \dfrac{1}{2}D_{ii} = \tau_{mn}S_{nm} \end{array} \right\} \tag{44}$$

The first of the terms on the right of equation (43) is the Rotta "tendency toward isotropy" term (ref. 15), involving the departure from isotropy of the normal Reynolds stresses. The remaining terms represent the interaction between the Reynolds stresses and the mean flow. While some of the elements in these terms (refer to equations (44)), are similar to the unmodeled production terms, the terms are structured to vanish when the trace of Φ_{ij} is taken, as would be required by continuity for an incompressible fluid within equation (42). The relationship of these terms to production and dissipation of the Reynolds stresses can be demonstrated most directly by introducing the mean rate of strain and vorticity tensors (eqs. (8) and (21)), respectively. For example, the exact production terms in equation (35) can then be rewritten as

$$\tau_{im}\frac{\partial u_j}{\partial x_m} + \tau_{jm}\frac{\partial u_i}{\partial x_m} = (\tau_{jm}S_{mi} + \tau_{im}S_{mj}) + (\tau_{jm}\Omega_{mi} + \tau_{im}\Omega_{mj}) \tag{45}$$

(total production)   (production due to straining)   (production due to rotation)

If the strain and vorticity tensors are introduced into equation (43), and this general pressure strain correlation is introduced into equation (35), there results for incompressible flow

$$\frac{D\tau_{ij}}{Dt} = (\tau_{im}S_{mj} + \tau_{jm}S_{mi})(-1 + \hat{\alpha} + \hat{\beta}) - (\tau_{im}\Omega_{mj} + \tau_{jm}\Omega_{mi})(-1 + \hat{\alpha} - \hat{\beta})$$
$$- (\hat{\alpha} + \hat{\beta})\frac{2}{3}\delta_{ij}P + \beta^* \omega e \left[\frac{2}{3}\delta_{ij} - C_1\left(\frac{\tau_{ij}}{e} + \frac{2}{3}\delta_{ij}\right)\right]$$
$$+ \dot{\gamma}eS_{ij} + \frac{\partial}{\partial x_k}\left[(\nu + \sigma^*)\frac{\partial \tau_{ij}}{\partial x_k}\right] \tag{46}$$

This form of the Reynolds stress equations is equivalent to that given in reference 16, but the coefficients used in each case have slightly different definitions which causes some apparent sign differences.

From equation (46) it is seen that the pressure rate of strain correlation terms, identified by the modeling constants C_1, α, and $\hat{\beta}$, behave in parallel with the production and dissipation terms; the $\hat{\alpha}$ and $\hat{\beta}$ complement the factor -1 in the first two production terms resulting from strain and rotation, and part of C_1 can be considered to account for some anisotropic dissipation. When equation (46) is applied to a flow with uniform shearing strain, where

12

$$S_{12} = \frac{1}{2}\frac{\partial u_1}{\partial x_2} = S_{21}$$
$$\Omega_{12} = \frac{1}{2}\frac{\partial u_1}{\partial x_2} = -\Omega_{21} \Bigg\} \tag{47}$$

are the only nonzero elements of the strain and vorticity tensors and when convection and diffusion are neglected, there results

$$\frac{\tau_{11}}{e} + \frac{2}{3} = \frac{-4 + 4\hat{\alpha} - 2\hat{\beta}}{3C_1} \tag{48}$$

$$\frac{\tau_{22}}{e} + \frac{2}{3} = \frac{2 - 2\hat{\alpha} + 4\hat{\beta}}{3C_1} \tag{49}$$

and

$$\frac{\tau_{33}}{e} + \frac{2}{3} = \frac{2 - 2\hat{\alpha} - 2\hat{\beta}}{3C_1} \tag{50}$$

The corresponding shearing stress is

$$\frac{\tau_{12}}{e} = \sqrt{\frac{(\hat{\alpha} - 1)(\tau_{22}/e) + \hat{\beta}(\tau_{11}/e) + (\hat{\gamma}/2)}{C_1}} \tag{51}$$

Because equations (48) through (50) are not independent, these equations, together with equation (51), cannot in themselves be used with specified values of the normal and shear Reynolds stresses to define the four constants $\hat{\alpha}$, $\hat{\beta}$, $\hat{\gamma}$, and C_1. Launder et al. (ref. 14) avoided this difficulty by following Rotta's (ref. 15) suggestion regarding tensor symmetries of the pressure strain terms and found that $\hat{\alpha}$, $\hat{\beta}$, $\hat{\gamma}$ could each be expressed in terms of a pair of constants, C_1 and C_2. They then employed experimental data of the normal Reynolds stresses in nearly homogeneous shear flows to define C_1 and C_2 through equations equivalent to equations (48) through (50). The approach in the present analysis is to require consistency between equations (48) through (51) with equations (31), (32), and (33). In addition, it is necessary to introduce the assumption that rotation alone does not cause a redistribution of the Reynolds stress. This assumption is consistent with the argument that eliminated the last term of equation (22). The Reynolds stress model of the present analysis, therefore, has been forced to be consistent with the previously developed two-equation model, where the normal stresses in the logarithmic region of the boundary layer were set in the ratio $\tau_{11}:\tau_{22}:\tau_{33} = 4:2:3$. The values of $\hat{\alpha}$, $\hat{\beta}$, $\hat{\gamma}$, and C_1 resulting from this model are given in table 1 along with the values used by Launder et al. (not including special near-wall effects).

13

TABLE 1.- COMPARISON OF CLOSURE COEFFICIENTS IN REYNOLDS STRESS MODELS

Model	Coefficient			
	C_1	$\hat{\alpha}$	$\hat{\beta}$	$\hat{\gamma}$
Present study	4.5	0.5	0.5	1.33
Launder, Reese, and Rodi	1.5	.76	.11	.36

The values of the Reynolds stress components in the logarithmic region of a flat plate boundary layer utilized in the present model are compared to the corresponding values of the model of reference 14 in table 2.

TABLE 2.- REYNOLDS STRESS COMPONENTS IN THE LOGARITHMIC REGION
OF A FLAT PLATE BOUNDARY LAYER

Model	Reynolds stress component			
	τ_{11}/e	τ_{22}/e	τ_{33}/e	τ_{12}/e
Present study	-0.89	-0.44	-0.66	0.31
Launder, Reese, and Rodi	- .93	- .46	- .61	.35

A comparison of these tables reveals that similar values of Reynolds stress components can be achieved in a nearly homogeneous shear layer or in the logarithmic region of a boundary layer with rather disparate sets of modeling coefficients based on different physical arguments. For example, the physical assumption that mean flow rotation has no effect on the redistribution of the Reynolds stresses force $\hat{\alpha} = \hat{\beta}$, and the consequence of this is felt in all the other coefficients. One result is that the present model places greater emphasis on the Rotta term, through the larger C_1, than does the Launder model. Obviously, these models must be tested against data in flows that are different from a nearly homogeneous shear layer to determine which model has the better universal character. It is interesting to note that, in terms of the symbols used in the present model, $C_1 = \lambda*/\beta*$. With these modeling constants it can be shown that in a uniform shear flow

$$\tau_{12} = - \frac{2}{9\beta*} \frac{\tau_{22}}{\omega} \frac{\partial u_1}{\partial x} \tag{52}$$

Equation (52) is equivalent to an eddy diffusivity formulation and provides a justification for the use of such a concept in nearly uniform shear layers. It is interesting, however, that the "eddy diffusivity" is proportional to τ_{22} rather than to e as in the two-equation model. This difference proves extremely important for flows over curved surfaces (ref. 17) and is exploited in a later section of this report.

14

APPLICATION TO TURBULENT FLOWS WITH PLANE STRAIN AND UNIFORM SHEAR

In the first series of tests of the two revised models, consideration is given to the distortion of high Reynolds number ($Re_T \gg 1$) grid turbulence caused by an application of plane strain and uniform shear. These cases act as tests of the models where near-wall viscous effects are unimportant. For these flows the velocity gradient tensor simplifies to

$$\frac{\partial u_i}{\partial x_j} = \begin{bmatrix} \bar{\varepsilon} & \bar{\kappa} & 0 \\ 0 & \bar{\varepsilon}f & 0 \\ 0 & 0 & -(1+f)\bar{\varepsilon} \end{bmatrix} \tag{53}$$

where $\bar{\varepsilon}$ and $\bar{\kappa}$ are the axial strain rate and shearing rate, respectively. The 11 cases considered are indicated in table 3.

TABLE 3.- PLANE STRAIN AND UNIFORM SHEAR TEST CASES

Reference	$\bar{\varepsilon}(sec^{-1})$	$\bar{\kappa}(sec^{-1})$	f	$\beta\omega_o$	t_{max}
Tucker-Reynolds (ref. 12)	4.45	0.0	0	21.5	0.400
Reynolds-Tucker (ref. 18)	4.80		0		.220
	14.00		0		.135
	12.00		-1/2		.145
	3.25		1		.255
Townsend (ref. 19)	9.41		0	70.00	.150
Marechal (ref. 20)	19.00		0	60.00	.135
Uberoi (ref. 21)	7.62		-1/2	13.5	.180
	18.20		-1/2		.120
	32.50		-1/2		.086
Champagne-Harris-Corrsin (ref. 22)	0.00	12.9	0		.176

The assumption that the turbulence is homogeneous in a coordinate system that moves with the fluid volume, leads to the expression of the two-equation model in the following simple form:

$$\frac{de}{dt} = \{(-u'v')\,\bar{\kappa} + [\langle w'^2\rangle\,(1+f) - \langle v'^2\rangle\,f - \langle u'^2\rangle]\bar{\varepsilon}\} - \beta^{\star}\omega e \tag{54}$$

$$\frac{d\omega^2}{dt} = \gamma_\infty \frac{\omega^2}{e}\,\{(-u'v')\,\bar{\kappa} + [\langle w'^2\rangle\,(1+f) - \langle v'^2\rangle\,f - \langle u'^2\rangle]\bar{\varepsilon}\} - \beta\omega^3 \tag{55}$$

where

$$\frac{\langle -u'v' \rangle}{e} = \frac{\bar{\kappa}}{\omega} \tag{56}$$

$$\frac{\langle u'^2 \rangle}{e} = \frac{2}{3} - 2 \frac{\bar{\epsilon}}{\omega} + \frac{4}{9\beta^*} \frac{(\bar{\kappa}/\omega)^2}{1 + \chi^2} \tag{57}$$

$$\frac{\langle v'^2 \rangle}{e} = \frac{2}{3} - 2 \frac{\bar{\epsilon}}{\omega} f - \frac{4}{9\beta^*} \frac{(\bar{\kappa}/\omega)^2}{1 + \chi^2} \tag{58}$$

$$\frac{\langle w'^2 \rangle}{e} = \frac{2}{3} + 2 \frac{\bar{\epsilon}}{\omega} (1 + f) \tag{59}$$

and

$$\chi^2 = \frac{4(\bar{\epsilon}/\omega)(1 + f + f^2) + (\bar{\kappa}/\omega)^2}{\beta^*} \tag{60}$$

Note that in writing equations (54) to (60) the turbulent Reynolds number is assumed very large so that viscous effects are ignored. The RSE model simplifies in a similar manner, although the equations are more lengthy; for brevity the simplified RSE model equations are not presented.

The computations of the ordinary differential equations have been performed with a fourth-order Runge-Kutta integration scheme. To initiate the computations, a value for the dissipation rate, ω, is needed at $t = 0$. For the Tucker-Reynolds experiment, the initial value of ω has been determined from the measured variation of e upstream of the straining region. That is, in the absence of strain, e is given by

$$\frac{e}{e_{ref}} = \left[1 + \frac{1}{2} \beta\omega_{ref} (t - t_{ref}) \right]^{-6/5} \tag{61}$$

where subscript ref denotes reference conditions. From the known variation of e with $t = x/U$, the value of ω_{ref} and hence ω at the initial station has been determined to be

$$\beta\omega_o = 21.5 \text{ sec}^{-1} \tag{62}$$

To set $\beta\omega_o$ for the other flows, we have used values similar to those used by Saffman (ref. 9) but with slight differences.

Of the eleven cases considered, the Tucker-Reynolds (ref. 12), Champagne-Harris-Corrsin (ref. 22), and Townsend (ref. 19) experiments are the most completely documented. Hence, we first focus on these three cases.

Tucker-Reynolds Plane Strain Flow

Figure 1 compares the computed and measured distortion parameter, K, for the Tucker-Reynolds plane strain flow; by definition

16

$$K \equiv \frac{\langle w'^2 \rangle - \langle u'^2 \rangle}{\langle w'^2 \rangle + \langle u'^2 \rangle} \tag{63}$$

As shown, good agreement has been obtained between computed and measured values of K when the RSE model is used. Note that the postulated variation of λ_∞^* with the strain parameter χ (see eqs. (39)), viz,

$$\lambda_\infty^* = \left[\frac{9}{2} - \frac{5}{2} \exp(-5\chi) \right] \beta^* \tag{64}$$

is needed to insure the proper relaxation of the anisotropy after the strain is removed. Although a less rapid variation of λ_∞^* with χ is acceptable for this flow, equation (64) has been found most suitable overall for all the flows considered. Figure 2 shows how close the RSE model predicted normal Reynolds stresses are to the corresponding measured stresses when the initially anisotropic character of the flow is accounted for.

Results obtained using the two-equation model are not in as close agreement with the data. At the onset and termination of strain, discontinuous jumps in the stresses occur. For example, when the strain is removed, the two-equation model unrealistically predicts an instantaneous return to isotropy. Also, the predicted value of K at the end of the straining region is only 0.39 compared to the corresponding measured value of between 0.55 and 0.65.

As a numerical experiment, the two-equation model computation was continued much farther downstream without removing the strain. The asymptotic value of the distortion parameter is 0.55, a value nearly identical to that predicted by the RSE model. Additionally, it was found that when the Saffman production terms are used the asymptotic value is 0.675. With either type of production term, the asymptotic value is not achieved until about $x = 7.6$ m. The results of this numerical experiment and the fact that the two-equation model predicts an abrupt return to isotropy when the strain is removed illustrate the fact that even with *the new constitutive relation (eq. (20)), the two-equation eddy viscosity model is limited to near-equilibrium flow conditions.*

Champagne-Harris-Corrsin Uniform Shear Flow

Figure 3 compares computed and measured Reynolds stresses for the Champagne, Harris, and Corrsin uniform shear flow. The entire region of developing flow is considered, not merely the asymptotic values. As shown, the RSE model predicted stresses that are in relatively close agreement with the data. At $x = 3.2$ m the computed shape parameter, $\langle -u'v' \rangle / \sqrt{\langle u'^2 \rangle \langle v'^2 \rangle}$, of 0.47 is 2% lower than the measured value. The only noticeable disagreement occurs between computed and measured values for $\langle w'^2 \rangle$; the model predicts that as the flow approaches equilibrium,

$$\frac{\langle w'^2 \rangle}{e} \doteq \frac{2}{3} \tag{65}$$

while the data indicate a ratio of 0.574, somewhat closer to values used by Launder, Reese, and Rodi (see table 2). This is a consequence of the fact that the model predicts that in equilibrium the normal stresses lie in the ratio

17

$$\langle u'^2 \rangle : \langle v'^2 \rangle : \langle w'^2 \rangle = 4:2:3 \tag{66}$$

while the data indicate

$$\langle u'^2 \rangle : \langle v'^2 \rangle : \langle w'^2 \rangle = 4:2:2.4 \tag{67}$$

As with the Tucker-Reynolds computation, the two-equation model predicts a slower approach to equilibrium than does the RSE model and the data. Again, it is instructive to examine the asymptotic solution for the two-equation model with the conventional and with the Saffman production terms. We find the following:

$$\frac{\langle -u'v' \rangle}{\sqrt{\langle u'^2 \rangle \langle v'^2 \rangle}} \rightarrow \begin{cases} 0.48, & \text{conventional production} \\ 0.76, & \text{Saffman production} \end{cases} \tag{68}$$

and

$$\langle u'^2 \rangle : \langle v'^2 \rangle : \langle w'^2 \rangle \rightarrow \begin{cases} 4:2:3, & \text{conventional production} \\ 4:1.5:3, & \text{Saffman production} \end{cases} \tag{69}$$

Compared with equation (67), equation (69) provides another argument against using the Saffman production terms. On the one hand, using the Saffman production terms yields a normal stress ratio of 4:2:3 for a flat plate boundary layer (FPBL). This ratio occurs because the turbulent mixing energy production and dissipation terms balance. However, for the Champagne, Harris, and Corrsin flow the balance occurs in the ω equation rather than the e equation when the Saffman terms are used; consequently the normal stress ratio is distorted. On the other hand, using the conventional production terms leads to a production-dissipation balance in the e equation both for the Champagne, Harris, and Corrsin flow and for flat plate boundary-layer flow. Since the RSE model and the Champagne et al. data also indicate that turbulent energy production and dissipation balance, using conventional production terms appears to yield a more suitable physical representation for uniform shear flow.

Townsend Plane Strain Flow

Figure 4 compares the computed and measured distortion parameters for Townsend's (ref. 19) plane strain flow. Again, reasonably close agreement between RSE computed and measured values of K have been obtained. With the two-equation model, predicted values of K are about 25% lower than measured.

Other Plane Strain Flows

Figure 5 presents a summary of computed and measured distortion parameters for the ten plane strain flows listed in table 3. Only RSE model predictions are shown in the figure. As shown, the predicted values of K at $t = t_{max}$ (the time corresponding to the farthest downstream station) lie within 20% of

18

corresponding measured values (see table 3). The two-equation model generally predicts values of K which are about 70% of measured. The agreement with data of long-time asymptotic values is much better, further illustrating the fact that the two-equation model fails to accurately describe the rate of approach to equilibrium.

NEAR-WALL VISCOUS MODIFICATIONS

The conservation and turbulence model equations presented earlier contained terms involving the molecular viscosity of the fluid in order to permit boundary-layer computations with integration through the viscous sublayer and no-slip boundary conditions. In this way, use of artificial boundary conditions such as the "law of the wall" can be avoided and the uncertainties of such boundary conditions far from flat plate boundary-layer conditions can be eliminated. For the mean conservation equations it is sufficient to include molecular viscosity in the diffusion terms. Similarly, the use of molecular diffusion in the various model equations permits imposition of the no-slip condition on the Reynolds stress and turbulent heat flux as well as on the mean velocity, that is,

$$u_i = q_i = \tau_{ij} = 0 \quad \text{at} \quad y = 0 \tag{70}$$

However, without further modification it was found by using the sublayer program developed by Wilcox and Traci (ref. 6) that the smooth-wall value of the constant in the law of the wall, C, defined by

$$C = \lim_{(u_\tau y/\nu) \to \infty} \left(\frac{u}{u_\tau} - \frac{1}{\kappa} \log \frac{u_\tau y}{\nu} \right) \tag{71}$$

is approximately 7.0 and 7.5 for the two-equation and RSE models, respectively. As these values differ from the commonly accepted value of C between 5.0 and 5.5, further viscous modifications were indicated. Wilcox and Traci (ref. 6) have shown that a proper level of C could be achieved by introducing viscous damping of the production terms in the e and ω equation. This result can be accomplished in the present models by damping the Reynolds shear stress, which is implemented in the revised two-equation model by writing

$$\epsilon = \frac{\gamma^* e}{\omega} \tag{72}$$

where

$$\gamma^* = 1 - (1 - \lambda^2)\exp(-Re_T/R_e) \tag{73}$$

To allow a different rate of damping of the ω equation production term, we also write

$$\gamma\gamma^* = \gamma_\infty[1 - (1 - \lambda^2)\exp(-Re_T/R_\omega)] \tag{74}$$

where $\gamma_{\infty} = 10/9$ is the high Reynolds number value of γ. The closure coefficients λ, R_e and R_{ω} are similar to those introduced by Wilcox and Traci (ref. 6).

For the Reynolds stress model, the Reynolds stress itself is damped by increasing λ^* as follows:

$$\lambda^* = \lambda_{\infty}^*[1 - (1 - \lambda^2)\exp(-Re_T/R_e)]^{-1} \tag{75}$$

while γ is modified according to

$$\frac{\gamma}{\lambda^*} = \frac{\gamma_{\infty}}{\lambda_{\infty}^*} [1 - (1 - \lambda^2)\exp(-Re_T/R_{\omega})] \tag{76}$$

where three closure coefficients λ, R_e, and R_{ω} again appear. To set the value of λ, we demand that in a Blasius boundary layer the models predict that turbulent fluctuations are damped for Reynolds numbers below the linear-stability theory, minimum-critical Reynolds number, $Re_c = 9 \times 10^4$. Turbulent fluctuations are damped provided turbulent energy production $\tau \, \partial u/\partial y$ is less than dissipation, $\beta^* \omega e$. This condition is satisfied throughout the boundary layer up to a plate-length Reynolds number $Re_{\hat{x}}$, given by

$$Re_{\hat{x}} = \begin{cases} \dfrac{750}{\lambda^2} & , \quad \text{two-equation model} \\[3mm] \dfrac{456}{\lambda^2(1 - \lambda^2/3)} & , \quad \text{RSE model} \end{cases} \tag{77}$$

Requiring $Re_{\hat{x}} = Re_c$ yields the following values for λ:

$$\lambda = \begin{cases} \dfrac{1}{11} & , \quad \text{two-equation model} \\[3mm] \dfrac{1}{14} & , \quad \text{RSE model} \end{cases} \tag{78}$$

Following Wilcox and Traci, sublayer solutions have been obtained to determine loci of values (R_e, R_{ω}) which yield a smooth-wall value for C of 5.5. As shown in figure 6, such a locus exists for each model. To select the optimum (R_e, R_{ω}) pair, the turbulent energy balance between production and dissipation has been compared with Laufer's (ref. 23) sublayer data (fig. 7). Closest agreement with the data[3] is obtained by using

$$R_e = 1 ; \quad \text{both models} \tag{79}$$

and

$$R_{\omega} = \begin{cases} 2 ; & \text{two-equation model} \\[2mm] 3 ; & \text{RSE model} \end{cases} \tag{80}$$

---

[3]To further validate the choices for R_e and R_{ω}, a few flat plate boundary-layer transition predictions have been made. Transition location and width are roughly the same as predicted with the Wilcox-Traci model. Although further testing will be needed, it appears that the two revised models probably predict transition as well as the Wilcox-Traci model and that transition modifications devised by Wilcox (ref. 24) apply to both of these models.

20

EQUILIBRIUM BOUNDARY-LAYER APPLICATIONS

In these applications, the turbulence models are used to compute three well documented near-equilibrium boundary layers under incompressible flow conditions. The models are then applied to a compressible, flat plate boundary layer. Then, an example of a compressible boundary layer is computed to demonstrate the effects of relatively strong adverse and favorable pressure gradients. These computations are compared with both surface and profile data.

Incompressible Flows

To provide definitive tests of the revised models, flows were selected (table 4) which include experimental data for all of the Reynolds stress components. Of the three cases, the low Reynolds number of the Andersen adverse-pressure gradient case provides the most rigorous test of the models' ability to simulate viscous effects.

TABLE 4.- BOUNDARY-LAYER EXPERIMENTS USED TO ASSESS THE TURBULENCE MODELS

Flow	Data sources
Flat plate boundary layer	Karman-Schoenherr (ref. 25) skin-friction correlation; Klebanoff (ref. 26) data; Wieghardt (ref. 27) data.
Bradshaw adverse pressure gradient	Bradshaw (ref. 28) data; Coles (ref. 27) version of Bradshaw data.
Andersen adverse pressure gradient	Andersen (ref. 29) data.

Figures 8 to 10 compare computed and measured skin friction, c_f, and shape factor, H, along the three equilibrium boundary layers. Over these three experiments, both models predict values of skin friction that are generally within 5% of the data on both the flat plate and in adverse pressure gradients. The predictions are lower than the data, with the RSE model yielding slightly lower values than the two-equation model. The computed shape factors are within 3% of the measured values for the two-equation model and within 5% when the RSE model is used.

The predicted velocity profiles for both models are compared with the data of the three experiments in figures 11 to 13. In figure 11 (the flat plate boundary layer), the computations show a slightly thinner boundary layer than given by the data, with the larger differences occurring at the low Reynolds number. Generally, the values of u^+ are within 5% of the measured values. For the test cases with adverse pressure gradients, the computations yield velocity profiles that are generally less full than the data, but within 20% of the experimental values of u^+ even for the poorest comparisons (with

21

the original Bradshaw data or Anderson's 1.8 m station). In these figures, there is little choice between the two-equation and Reynolds stress models.

The computed and measured Reynolds stresses are compared in figures 14 to 16, where the mean velocity profiles are also displayed as u/U_e versus y/δ. For all three flows, both models predict all four Reynolds stresses to within 10% of the measured values, except in the regions closest to the surface. This is not surprising when it is recalled that the modeling coefficients were based on arguments that in the law of the wall region both the turbulent shear and kinetic energy are constant with y (refer to eq. (32) and (33) or eq. (51)), whereas the data actually show variations of about 30% in e. Changes very close to the surface in the current model, along the lines taken by Launder et al. (ref. 14), possibly would improve this situation. It is reassuring, however, that the normal stress component most accurately predicted is $\langle v'^2 \rangle$ or τ_{22}, and in view of equation (52) explains why the shear stress in the present model is predicted rather accurately even though e is not. In the normalized mean velocity profiles, the RSE model velocity profiles appear to have suffered more deceleration than those of the two-equation model. On balance, the two-equation model shows slightly closer agreement with the boundary-layer data than does the RSE model.

Compressible Flow

The turbulence models presented here were extended to compressible flow through the assumption that the effects of compressibility can be introduced primarily by use of the Favre mass-weighted dependent variables (ref. 30) in both the conservation and modeling equations. When Wilcox and Alber (ref. 4) first utilized the Favre variables they noted additional terms entered the modeling equations that were explicitly dependent on the compressibility of the fluid. Also, they suggested that the dissipation rate would require some scaling on density to assure proper representation of the compressible terms. Later, Rubesin (ref. 31) analyzed how the additional compressibility terms in the kinetic energy could be further modeled. Experience with the latter model (ref. 32), however, showed that reasonable comparison with data could be achieved if these supplemental terms were ignored. This, together with the rather successful experience with the Wilcox-Traci two-equation model (ref. 7), which also does not use these terms, led to the neglect of extra compressibility terms in the present model.

The scaling introduced by compressibility in the present model can be illustrated by an analysis of the behavior of the two-equation model in the near-wall region of compressible boundary layer on a flat plate. Emphasis will be placed on the "law-of-the-wall" region, where it is permissible to neglect convection and molecular diffusion. The momentum equation (eq. (4)) reduces to

$$\rho \varepsilon \frac{\partial u}{\partial y} = \rho_w u_\tau^2 \tag{81}$$

and the model equations simplify to

22

$$0 = \rho\varepsilon\left(\frac{\partial u}{\partial y}\right)^2 - \beta^*\rho\omega e + \sigma^* \frac{\partial}{\partial y}\left(\rho\varepsilon \frac{\partial e}{\partial y}\right) \tag{82}$$

and

$$0 = \gamma \frac{\omega^2}{e}\, \rho\varepsilon\left(\frac{\partial u}{\partial y}\right)^2 - \left[\beta + 2\sigma\left(\frac{\partial \ell}{\partial y}\right)^2\right]\rho\omega^3 + \sigma \frac{\partial}{\partial y}\left(\rho\varepsilon \frac{\partial \omega^2}{\partial y}\right) \tag{83}$$

In the logarithmic region of the boundary layer, the turbulence Reynolds number is sufficiently high that

$$\left.\begin{array}{l} \gamma^* = 1 \\[2mm] \gamma = \dfrac{10}{9} \end{array}\right\} \tag{84}$$

Also, in this region (ref. 33),

$$\frac{u^*}{u_\tau} = \frac{1}{\kappa} \ln \frac{y u_\tau}{\nu_w} + B \tag{85}$$

where

$$u^* = \int_0^u \sqrt{\frac{\rho}{\rho_w}}\, du \tag{86}$$

In this boundary-layer region, a balance exists between the production and dissipation of the turbulence kinetic energy so that the diffusion term in equation (82) can also be neglected. From equations (12), (82), (85), and (86), it follows that

$$\omega \sqrt{\frac{\rho}{\rho_w}} = \frac{u_\tau}{\beta^{*1/2}\kappa y} \tag{87}$$

From equation (81), with equation (87), it is found that

$$\left(\frac{\rho}{\rho_w}\right)e = \frac{u_\tau^2}{\beta^{*1/2}} \tag{88}$$

Equations (87) and (88), therefore, represent the density scaling inherent in the momentum and turbulence mixing energy model equations. The scaling question would be closed if the forms in the above equations would als satisfy the specific dissipation rate equation. When equations (85) through (88) are substituted into equation (83) there results

$$0 = \gamma\beta^{*1/2} - \left(\frac{\beta}{\beta^{*1/2}} + 2\sigma\kappa^2\right) + 2\sigma\kappa^2\left[2 + 0\left(\frac{u_\tau}{u_e}\right) f\left(M_e,\ \frac{T_w}{T_3}\right) + \ldots\right] \tag{89}$$

Thus in the limit of the infinitely high Reynolds number where $u_\tau/u_e \to 0$, the last term vanishes and the usual incompressible flow interrelationship between the modeling coefficients results. Therefore, equation (83) is satisfied for high Reynolds number, indicating that the density scaling represented by

23

equations (87) and (88) satisfies both the modeling equations and the momentum equation in the logarithmic region of a boundary layer. It is interesting that in this boundary-layer region the length scale is

$$\ell = \frac{e^{1/2}}{\omega} = \beta*^{1/4} \kappa y \tag{90}$$

and identical to that which exists in an incompressible flow.

Calculations of the boundary-layer skin friction on an adiabatic flat plate at Mach numbers up to five and for cooled wall conditions at a Mach number equal to five are compared with results from the van Driest II formulas in figures 17 and 18. These formulas have been shown (ref. 34) to represent the bulk of existing data under these conditions to about ±10%. The agreement between the methods is excellent, but this is not surprising in view of the similarity of the density scaling indicated by equations (87) and (88) and that which is inherent in the van Driest formulas. What differences exist are largely due to the density scaling differences inherent in the wake region of the boundary layer. For these flat plate conditions, both the two-equation and RSE models yield essentially the same results.

An example of a more severe test of the models for compressible flow is the boundary-layer experiment at a Mach number of four conducted by Lewis, Gran, and Kubota (ref. 35). In this experiment, an axisymmetric turbulent boundary layer on the adiabatic interior wall of a circular cylinder was subjected to an adverse pressure gradient followed by a favorable pressure gradient. These pressure gradients were achieved by means of a shaped centerbody. The distribution of the surface pressure is shown in figure 19. A pressure rise of nine times the upstream pressure was attained before pressure relaxation occurred. For reference, the circled numbers along the abscissa designate stations at which profile data will be compared in the figures that follow. The experimental data are primarily boundary-layer surveys of impact pressure and total temperature which are used to provide the mean velocity and density profiles at a sequence of stations. Local skin-friction coefficients were then obtained from Clauser plots of these data compared to equation (85). Turbulent shear profiles through the boundary layer were found from total shear profiles evaluated from changes in the stream direction of the mean momentum integrated from the surface to a point within the boundary layer. The error introduced by these methods permits assessment of the turbulence models to about ±15%.

Figure 20 shows the distribution of the surface skin-friction coefficient within the test zone. The coefficient shown is defined in terms of the upstream boundary-layer edge conditions rather than the local conditions and is therefore proportional to the surface shear. Along with the computed results based on the models presented here, computations based on the Marvin-Sheaffer code (ref. 36), which has been extended to contain a classic mixing length model essentially identical to that of Cebeci (ref. 37), are given for comparison. The mixing length model fails to capture the full rise of the skin friction caused by the adverse pressure gradient at these Mach numbers. On the other hand, it follows the data in the region of favorable pressure gradient quite well. The second-order closure models demonstrate a much

24

better prediction of the rise in skin friction in the adverse pressure gradient region; in the following favorable pressure gradient region, however, they show somewhat too large a drop in the skin friction. The two second-order models yield essentially equivalent results.

Figure 21 shows the distribution of the boundary-layer shape factor, $H = \delta^*/\theta$, along the test zone. The second-order models yield results that are close to the data. The results are generally better than those of the mixing length model except for the region immediately downstream of the station where the computations were initiated by matching the calculated and experimental momentum thicknesses.

Figures 22 through 27 show comparisons of the calculations based on the different turbulence models with mean velocity and turbulent shear profile data at the three stations designated in figure 19. Station 1 represents essentially flat plate conditions; station 2 is near the end of a long run of adverse pressure gradient; and station 3 is at the end of the favorable pressure gradient region. All of the models well represent the velocity profile at station 1. If one were to be favored, it would be the mixing length model which has been fine-tuned to represent equilibrium boundary layers. Figure 23 shows the turbulent shear profiles computed and measured at this station. Near the wall, the mixing length model overpredicts the shear by about 10%, whereas the second-order models are about 10% lower than the measurements. In the outer part of the boundary layer all the models yield results that are about 15% of the peak shear higher than the data. When consideration is given to the possible errors in the data, these comparisons are reasonably good and demonstrate that the second-order models generally give results in a zero pressure gradient as good as the fine-tuned mixing length model.

Figures 24 and 25 show the mean velocity and shear stress profiles at the station at the end of the adverse pressure gradient region. The experimental mean velocity data have become fuller in the vicinity of the surface, and the thickness of the boundary layer has been reduced relative to the data at the upstream station. All three models generally reflect this behavior, with the two-equation model showing the near-surface behavior best. Surprisingly, the RSE model does not show the near-wall fullness in the velocity profile even though it provides the best representation of the three models for the skin friction and local shear profile.

After the run of favorable pressure gradient, figure 26 shows the experimental mean velocity profile fuller and thicker than at the previously indicated station. All the models represent the experimental data quite well, with the second-order models showing a shade better agreement. The experimental shear stress profile at this station is now about an order of magnitude lower than the shear that existed at the previous station. Again the models show this drop in shear, however the second-order models overpredict the drop in shear in the inner part of the boundary layer. This is consistent with their skin-friction values at this station.

For this example of the behavior of a compressible boundary layer experiencing both adverse and favorable pressure gradients, it is concluded that the

25

second-order closure models, with modeling coefficients that are independent of the pressure gradients, represent the experimental data better than a mixing-length model with pressure gradient dependent modeling. This conclusion was also reached in references 38 and 39, where a broad range of compressible turbulent boundary-layer experiments were compared with the two-equation model for both attached and separated flows and with the RSE model for attached flows.

ADVANCED BOUNDARY-LAYER APPLICATIONS

The models presented here have been compared with the results of boundary-layer experiments designed to investigate special aspects of turbulence modeling. The effect of sudden application of transverse shear on the redistribution rate between the individual components of the Reynolds stress tensor was studied experimentally in references 40 and 41 and compared with our models in reference 42. The results of the comparison of the experimental data and the computations based on the models showed small improvement over a simple mixing-length model but still indicated a too-rapid rate of response to the transverse shear. It appears that the success of the RSE model for normally strained flows as indicated in figure 1 did not carry over as well to shearing strains.

Another application of the models has been to the problem of the effect of longitudinal curvature on turbulent boundary-layer behavior, the topic first recognized by Bradshaw (ref. 43). The Reynolds-stress equations were applied to this problem directly through conversion of the coordinates from Cartesian to curvilinear with one axis tangent to the body, s, and the other normal to the surface, n. The two-equation model, however, required a basic reinterpretation of the meaning of the symbol e, the kinetic energy term used earlier.

For flow over a streamwise curved surface with local radius of curvature R (convex, R > 0; concave, R < 0) the s,n curvilinear coordinate system introduces centrifugal and coriolis acceleration terms in the instantaneous equations of motion. In turn, these acceleration terms give rise to additional terms inversely proportional to R in the Reynolds stress equations. For a thin incompressible boundary layer these equations can be written as

$$u \frac{\partial \tau_{ss}}{\partial s} + v \frac{\partial \tau_{ss}}{\partial n} + 2 \frac{u}{R} \tau_{sn} = -2\tau_{sn} \frac{\partial u}{\partial n} + \frac{2}{3} \beta^\star \omega e - \lambda^\star \omega \left(\tau_{ss} + \frac{2}{3} e\right) + \tau_{sn}\left(\frac{\partial u}{\partial n} - \frac{u}{R}\right)$$

$$- \frac{2}{3} \tau_{sn}\left(\frac{\partial u}{\partial n} - \frac{u}{R}\right) + \frac{\partial}{\partial n} \left[\left(\nu + \sigma^\star \frac{e}{\omega}\right) \frac{\partial \tau_{ss}}{\partial n}\right] \quad (91)$$

$$u \frac{\partial \tau_{nn}}{\partial s} + v \frac{\partial \tau_{nn}}{\partial n} - 2 \frac{u}{R} \tau_{sn} = 2 \frac{u}{R} \tau_{sn} + \frac{2}{3} \beta^\star \omega e - \lambda^\star \omega \left(\tau_{nn} + \frac{2}{3} e\right) + \tau_{sn}\left(\frac{\partial u}{\partial n} - \frac{u}{R}\right)$$

$$- \frac{2}{3} \tau_{sn}\left(\frac{\partial u}{\partial n} - \frac{u}{R}\right) + \frac{\partial}{\partial n} \left[\left(\nu + \sigma^\star \frac{e}{\omega}\right) \frac{\partial \tau_{nn}}{\partial n}\right] \quad (92)$$

26

$$u \frac{\partial \tau_{zz}}{\partial s} + v \frac{\partial \tau_{zz}}{\partial n} = \frac{2}{3} \beta^* \omega e - \lambda^* \omega \left(\tau_{zz} - \frac{2}{3} e \right) - \frac{2}{3} \tau_{sn} \left(\frac{\partial u}{\partial n} - \frac{u}{R} \right)$$

$$+ \frac{\partial}{\partial n} \left[\left(\nu + \sigma^* \frac{e}{\omega} \right) \frac{\partial \tau_{zz}}{\partial n} \right] \tag{93}$$

$$u \frac{\partial \tau_{sn}}{\partial s} + v \frac{\partial \tau_{sn}}{\partial n} + \frac{u}{R} (\tau_{nn} - \tau_{ss}) = -\frac{u}{R} (\tau_{nn} - \tau_{ss}) - \tau_{nn} \left(\frac{\partial u}{\partial n} - \frac{u}{R} \right) - \lambda^* \omega \tau_{ns}$$

$$+ \left(\frac{\tau_{nn}}{2} + \frac{\tau_{ss}}{2} + \frac{2}{3} e \right) \left(\frac{\partial y}{\partial n} - \frac{u}{Rh} \right)$$

$$+ \frac{\partial}{\partial n} \left[\left(\nu + \sigma^* \frac{e}{\omega} \right) \frac{\partial \tau_{sn}}{\partial n} \right] \tag{94}$$

In these equations, terms with common factors have not been combined in order to reveal the physical source of the individual terms, that is, production, redistribution, etc. The sum of equations (91) through (93) yields the kinetic energy equation

$$u \frac{\partial e}{\partial s} + v \frac{\partial e}{\partial n} = \tau_{sn} \left(\frac{\partial u}{\partial n} - \frac{u}{R} \right) - \beta^* e \omega + \frac{\partial}{\partial n} \left[\left(\nu + \sigma^* \frac{e}{\omega} \right) \frac{\partial e}{\partial n} \right] \tag{95}$$

The specific dissipation rate equation is

$$u \frac{\partial \omega^2}{\partial s} + v \frac{\partial \omega^2}{\partial n} = \gamma \frac{\omega^2}{e} \tau_{sn} \left(\frac{\partial u}{\partial n} - \frac{u}{R} \right) - \left[3 + 2\sigma \left(\frac{\partial \ell}{\partial n} \right)^2 \right] \omega^3 + \frac{\partial}{\partial n} \left[\left(\nu + \sigma \frac{e}{\omega} \right) \frac{\partial \omega^2}{\partial n} \right] \tag{96}$$

Equations (91) through (96) were introduced into a boundary-layer code, and the results obtained from this code for comparison with some experimental data are given in the following figures. Before discussing these figures, however, it is interesting to examine the behavior of the Reynolds stress equations in the logarithmic region of the boundary layer where convection and diffusion terms can be neglected. Note that for this examination centrifugal forces are retained. Under these conditions,

$$\frac{\overline{(u')^2}}{e} = \frac{2}{3} + \frac{\beta^*}{\lambda^*} \frac{\frac{\partial u}{\partial n} + 3 \frac{u}{R}}{\frac{\partial u}{\partial n} - \frac{u}{R}} \tag{97}$$

$$\frac{\overline{(v')^2}}{e} = \frac{2}{3} - \frac{\beta^*}{\lambda^*} \frac{\frac{\partial u}{\partial n} + 3 \frac{u}{R}}{\frac{\partial u}{\partial n} - \frac{u}{R}} \tag{98}$$

$$\frac{\overline{(w')^2}}{e} = \frac{2}{3} \tag{99}$$

27

$$\frac{\tau}{e} = \sqrt{\frac{\beta^*}{\lambda^*}\left[\frac{2}{3} - \frac{\beta^*}{\lambda^*}\left(\frac{\frac{\partial u}{\partial n} + 3\,\frac{u}{R}}{\frac{\partial u}{\partial n} - \frac{u}{R}}\right)^2\right]} \qquad (100)$$

For a negative value of R, a concave surface, equations (97) to (100) show that, relative to the kinetic energy, u' is decreased, v' is increased, w' remains unchanged, and the shear stress τ is increased. A convex surface results in opposite behavior.

When equations (95) and (96) were utilized as the model equations for a two-equation model in the boundary-layer equations appropriate to longitudinally curved surfaces, it was found that the additional terms containing R did not produce the known curvature effects. This deficiency was corrected by exploiting the observations of the similar behavior of the shear stress and v' in the Reynolds stress equation in order to reinterpret the meaning of e for the two-equation model. As in references 1 and 17, e is thought of as a "mixing energy" rather than a "kinetic energy" and is defined as

$$e = -\frac{9}{4}\,\tau_{nn} \qquad (101)$$

With this definition for e and the forms of equations (92) and (95) as guidance, the e equation *for use with the two-equation model only* is written, in an *ad hoc* manner, as

$$u\,\frac{\partial e}{\partial s} + v\,\frac{\partial e}{\partial n} + \frac{9}{2}\,\frac{u}{R}\,\tau = \tau\left(\frac{\partial u}{\partial n} - \frac{u}{R}\right) - \beta^* e\omega + \frac{\partial}{\partial n}\left[(\nu + \sigma^*\varepsilon)\,\frac{\partial e}{\partial n}\right] \qquad (102)$$

with

$$\tau = \varepsilon\left(\frac{\partial u}{\partial n} - \frac{u}{R}\right)$$

where ε is given by equation (12) and the specific dissipation rate equation is equation (96). All the modeling coefficients and relationships employed in the two-equation model used earlier are retained. The third term on the left side of equation (102) represents the principal extra rate of strain introduced by the longitudinal curvature.

These model corrections for the effect of longitudinal surface curvature were tested against two boundary-layer flows experimentally measured by So and Mellor (ref. 44) over a convex surface. One flow was in a zero pressure gradient, whereas the second boundary layer experienced an adverse pressure gradient. Figures 28 through 33 compare the measured data with the computed results. Figures 28 and 29 compare measured skin friction and form factors with the computed results with and without accounting for the effect of longitudinal surface curvature. The computed results were matched to the first station by assuming the flow upstream of that station to be on a flat plate of a length to yield the correct skin friction there. For the case of the convex wall with constant pressure, the unmodified models show none of the drop in

28

skin friction experienced in the experiment. Except for their behavior immediately after the first station where the radius of curvature is suddenly introduced, the modified models give an excellent representation of the skin-friction behavior on the convex surface. This is rather remarkable for the two-equation model, when its *ad hoc* formulation is considered. Both modified models also well represent the rise in the form factor experienced by the data. For the case of the adverse pressure gradient (fig. 29) the unmodified models again do not show an adequate drop in the skin friction, whereas the modified models represent the skin-friction data quite well. The models with surface curvature corrections also represent the shape factor data in the adverse pressure gradient well.

In figures 30 and 31, the computations are compared with the mean streamwise velocity data in law-of-the-wall coordinates. The data correspond to the stations farthest downstream where skin friction was measured for the zero and adverse pressure gradient cases, respectively. The effect of the convex surface is to enlarge the contribution of the wake portion of the boundary layer. Both the RSE and two-equation models that account for the longitudinal curvature capture this behavior rather well for both cases of surface pressure distribution. Again, the added rate of strain in the energy equation of the two-equation model yields remarkably close agreement with the data — even somewhat better than the RSE model. Note that for the adverse pressure gradient flow the large RSE model differences from measurements are mainly due to the models' overpredicting c_f at the station chosen for comparing theory and experiment. Figures 32 and 33 provide a measure of how well each model predicts the various Reynolds stresses. Generally speaking, the RSE model predicted stresses are as far above the measured values as the two-equation model predicted stresses are below measured values. Interestingly, while the near-wall values are more closely simulated with the RSE model, the shapes are more closely simulated with the two-equation model.

<div align="center">CONCLUDING REMARKS</div>

The most significant result of the study is the observation that the two-equation model is as accurate a the RSE model for the class of boundary layers considered. Furthermore the new two-equation model constitutive relation permits accurate prediction of all components of the Reynolds stress tensor.

The RSE model holds a distinct advantage over the two-equation model for turbulent flows which experience sudden changes in the strain rate and/or shear. While the two-equation model accurately predicts equilibrium states, the rate of approach to equilibrium often is inaccurate. With the RSE model, both the rate of approach to equilibrium and the equilibrium state are accurately predicted.

Results obtained suggest two tentative conclusions. First, there appears to be little advantage in using the RSE model rather than the two-equation model for two-dimensional attached boundary layers. Second, for separating

flows and for flow subjected to abrupt changes in strain rate and/or shear, the RSE model may prove superior to the two-equation model.

Ames Research Center
    National Aeronautics and Space Administration
        Moffett Field, Calif., 94035, October 15, 1979

REFERENCES

1. Wilcox, D. C.; and Chambers, T. L.: Streamline Curvature Effects on Tur-
   bulent Boundary Layers. DCW-R-04-01, DCW Industries, 1975.

2. Wilcox, D. C.; and Chambers, T. L.: Computation of Turbulent Boundary
   Layers on Curved Surfaces. DCW-R-07-01, DCW Industries, 1976.

3. Saffman, P. G.: A Model for Inhomogeneous Turbulent Flow. Proc. Roy.
   Soc., London, vol. A317, no. 1530, 1970, pp. 417-433.

4. Wilcox, D. C.; and Alber, I. E.: A Turbulence Model for High Speed Flows.
   Proceedings of the 23rd Heat Transfer and Fluid Mechanics Institute,
   Northridge, Calif., June 14-16, 1972, pp. 231-252.

5. Saffman, P. G.; and Wilcox, D. C.: Turbulence Model Predictions for Tur-
   bulent Boundary Layers. AIAA Journal, vol. 12, no. 4, 1974,
   pp. 541-546.

6. Wilcox, D. C.; and Traci, R. M.: A Complete Model of Turbulence. AIAA
   Paper 76-351, July 1976.

7. Rubesin, M. W.; Crisalli, A. J.; Horstman, C. C.; Acharya, M.; and
   Lanfranco, M. J.: A Critique of Some Recent Second-Order Closure
   Models for Compressible Boundary Layers. AIAA Paper 77-128,
   January 1977.

8. Ludwieg, H.; and Tillman, W.: Untersuchungen über die Wandschubspannung
   in turbulenten Reibungsschichten. Ing.-Arch., vol. 17, 1949,
   pp. 288-299 (English translation in NACA TM 1285, 1950).

9. Saffman, P. G.: Development of a Complete Model for the Calculation of
   Turbulent Shear Flows. Paper presented at the 1976 Duke Turbulence
   Conference, Duke University, Durham, North Carolina, April 1976.

10. Jones, W. P.; and Launder, B. E.: The Prediction of Laminarization with
    a Two-Equation Model of Turbulence. Int. J. Heat Mass Transfer,
    vol. 15, 1972, pp. 301-314.

11. Escudier, M. P.: The Distribution of the Mixing Length in Turbulent Flows
    Near Walls. Rept. TWF/TN/1, Imperial College, London, 1965.

12. Tucker, H. J.; and Reynolds, A. J.: The Distortion of Turbulence by
    Irrotational Plane Strain. J. Fluid Mech., vol. 32, pt. 4, 1968,
    pp. 657-673.

13. Ibbetson, A.; and Tritton, D. J.: Experiments on Turbulence in Rotating
    Fluid. J. Fluid Mech., vol. 68, pt. 4, 1975, pp. 639-672.

14. Launder, B. E.; Reece, G. J.; and Rodi, W.: Progress in the Development of a Reynolds Stress Turbulence Closure. J. Fluid Mech., vol. 68, pt. 3, 1975, pp. 537–566.

15. Rotta, J. C.: Statistische Theorie nichthomogener Turbulenz. Zeitschrift fur Physik, vol. 129, no. 6, 1951, pp. 547–572 (in German).

16. Naot, D.: Rapid Distortion Solutions for a Stress Transport Turbulence Model in Contracting Flow. Phys. Fluids, 21 (5), 1978, pp. 752–756.

17. Wilcox, D. C.; and Chambers, T. L.: Streamline Curvature Effects on Turbulent Boundary Layers. AIAA J., vol. 15, no. 4, 1977, pp. 574–580.

18. Reynolds, A. J.; and Tucker, H. J.: The Distortion of Turbulence by General Uniform Irrotational Strain. J. Fluid Mech., vol. 68, pt. 4, 1975, pp. 673–693.

19. Townsend, A. A.: The Uniform Distortion of Homogeneous Turbulence. Quarterly Journal of Mechanics and Applied Mathematics, vol. 7, pt. 1, 1954, pp. 104–127.

20. Marechal, J.: Étude Expérimentale de la Déformation Plane d'une Turbulence Homogéne. J. de Méch, vol. 11, no. 2, 1972, pp. 263–294 (in French).

21. Uberoi, M. S.: Effect of Wind-Tunnel Contraction on Free-Stream Turbulence. J. Aeron. Sci., vol. 23, no. 8, 1956, pp. 754–764.

22. Champagne, F. H.; Harris, V. G.; and Corrsin, S.: Experiments on Nearly Homogeneous Turbulent Shear Flow. J. Fluid Mech., vol. 41, pt. 1, 1970, pp. 81–139.

23. Laufer, J.: The Structure of Turbulence in Fully Developed Pipe Flow. NACA Rep. 1174, 1954.

24. Wilcox, D. C.: A Model for Transitional Flows. AIAA Paper 77-126, January 1977.

25. Von Karman, T.: Turbulence and Skin Friction. J. Aero. Sci., vol. 1, no. 1, 1934, pp. 1–20.

26. Klebanoff, P. S.: Characteristics of Turbulence in a Boundary Layer with Zero Pressure Gradient. NACA Rep. 1247, 1955.

27. Coles, D. E.; Hirst, E. A.; and S. J. Kline, et al., eds. Proceedings: Computation of Turbulent Boundary Layers — 1968 AFOSR-IFP-Stanford Conference, Vol. II, Stanford University, California, Thermoscience Div., 1969.

28. Bradshaw, P.: The Response of a Constant-Pressure Turbulent Boundary Layer to the Sudden Application of an Adverse Pressure Gradient. ARC R&M 3575, 1969.

29. Andersen, P. S.; Kays, W. M.; and Moffat, R. J.: The Turbulent Boundary
    Layer on a Porous Plate: An Experimental Study of the Fluid Mechanics
    for Adverse Free-stream Pressure Gradients. Rept. HMT-15, Dept. Mech.
    Engr., Stanford University, California, 1972.

30. Favre, A.: Equations des Gaz Turbulents Compressibles. J. Mecan.,
    vol. 4, no. 3, 1965, pp. 361-390.

31. Rubesin, M. W.: A One-Equation Model of Turbulence for Use with the Com-
    pressible Navier-Stokes Equations. NASA TM X-73,128, 1976.

32. Viegas, J. R.; and Coakley, T. J.: Numerical Investigation of Turbulence
    Models for Shock-Separated Boundary-Layer Flows. AIAA J., vol. 16,
    no. 4, 1978, pp. 293-294.

33. van Driest, E. R.: Turbulent Boundary Layer in Compressible Fluids.
    J. Aero. Sci., vol. 18, no. 3, 1951, pp. 145-160.

34. Hopkins, E. J.; and Inouye, M.: An Evaluation of Theories for Predicting
    Turbulent Skin Friction and Heat Transfer on Flat Plates at Supersonic
    and Hypersonic Mach Numbers. AIAA J., vol. 9, no. 6, 1971,
    pp. 993-1003.

35. Lewis, J. E.; Gran, R. L.; and Kubota, T.: An Experiment on the Adiabatic
    Compressible Turbulent Boundary Layer in Adverse and Favorable
    Pressure-Gradients, J. Fluid Mech., vol. 51, pt. 4, 1972, pp. 657-672.

36. Marvin, J. G.; and Sheaffer, Y. S.: A Method for Solving the Nonsimilar
    Boundary-Layer Equations Including Foreign Gas Injection. NASA
    TN D-5516, 1969.

37. Cebeci, T.; and Smith, A. M. O.: Analysis of Turbulent Boundary Layers.
    Academic Press, New York, 1974.

38. Horstman, C. C.; Kussoy, M. I.; and Lanfranco, M. J.: An Evaluation of
    Several Compressible Turbulent Boundary-Layer Models: Effects of Pres-
    sure Gradient and Reynolds Number. AIAA Paper 78-1160, July 1978.

39. Viegas, J. R.; and Horstman, C. C.: Comparison of Multiequation Turbu-
    lence Models for Several Shock Separated Boundary Layer Interaction
    Flows. AIAA Paper 78-1165, July 1978.

40. Bissonnette, L. R.; and Mellor, G. L.: Experiments on the Behavior of an
    Axisymmetric Turbulent Boundary Layer with a Sudden Circumferential
    Strain. J. Fluid Mech., vol. 63, pt 2, 1974, pp. 369-413. (Also
    Ph.D. Thesis by Bissonnette, L. R., Princeton University, 1970.

41. Lohmann, R. P.: The Response of a Developed Turbulent Boundary Layer to
    Local Transverse Surface Motion. Paper No. 76-FE-3, J. Fluid Eng.,
    Trans. ASME, vol. 98, ser. I., no. 3, 1976, pp. 354-363. (Also Ph.D.
    Thesis, University of Connecticut, 1974.)

42. Higuchi, H.; and Rubesin, M. W.: Behavior of a Turbulent Boundary Layer Subjected to Sudden Transverse Strain. AIAA Paper 78-201, January 1978.

43. Bradshaw, P.: Effects of Streamline Curvature on Turbulent Flow. AGARD-AG-169, 1973.

44. So, R. M. C.; and Mellor, G. L.: An Experimental Investigation of Turbulent Boundary Layers Along Curved Surfaces. NASA CR-1940, 1972.
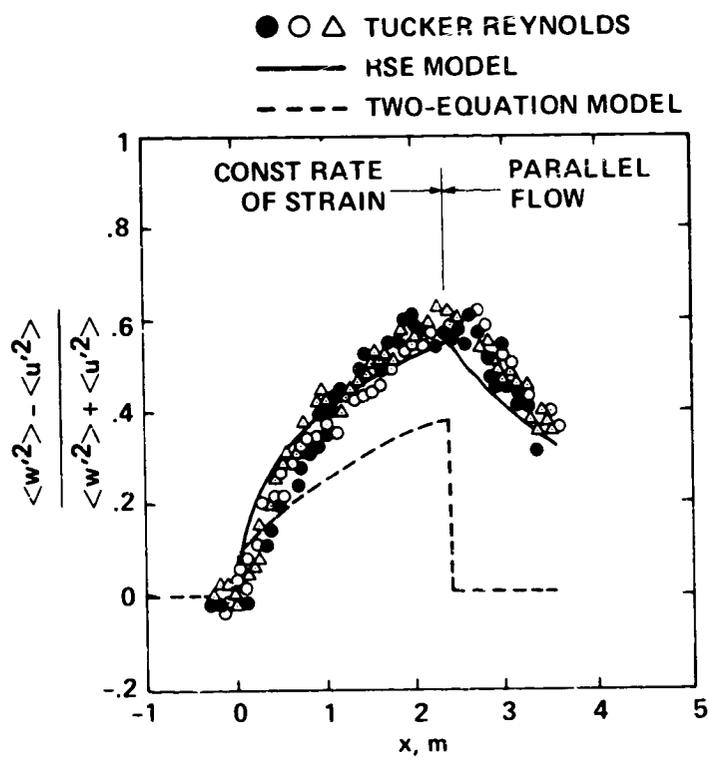
Figure 1.- Comparison of computed and measured distortion parameter for the Tucker-Reynolds plane strain flow.

35
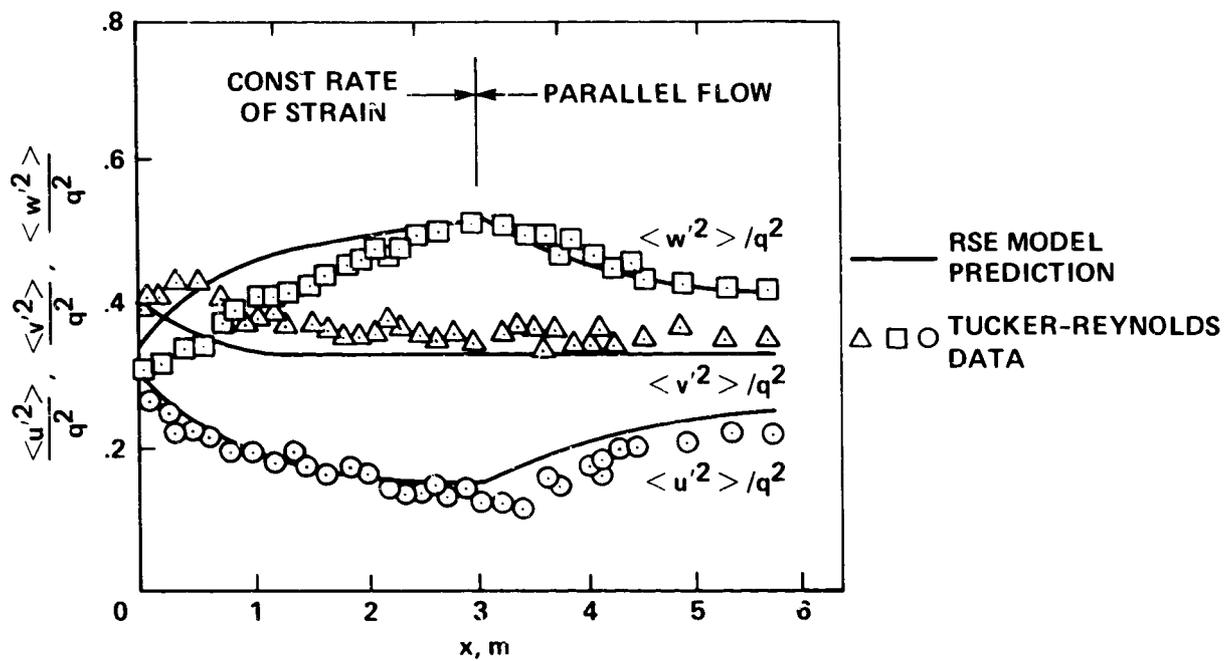
Figure 2.- Comparison of computed and measured normal Reynolds stresses for the Tucker-Reynolds plane strain flow.
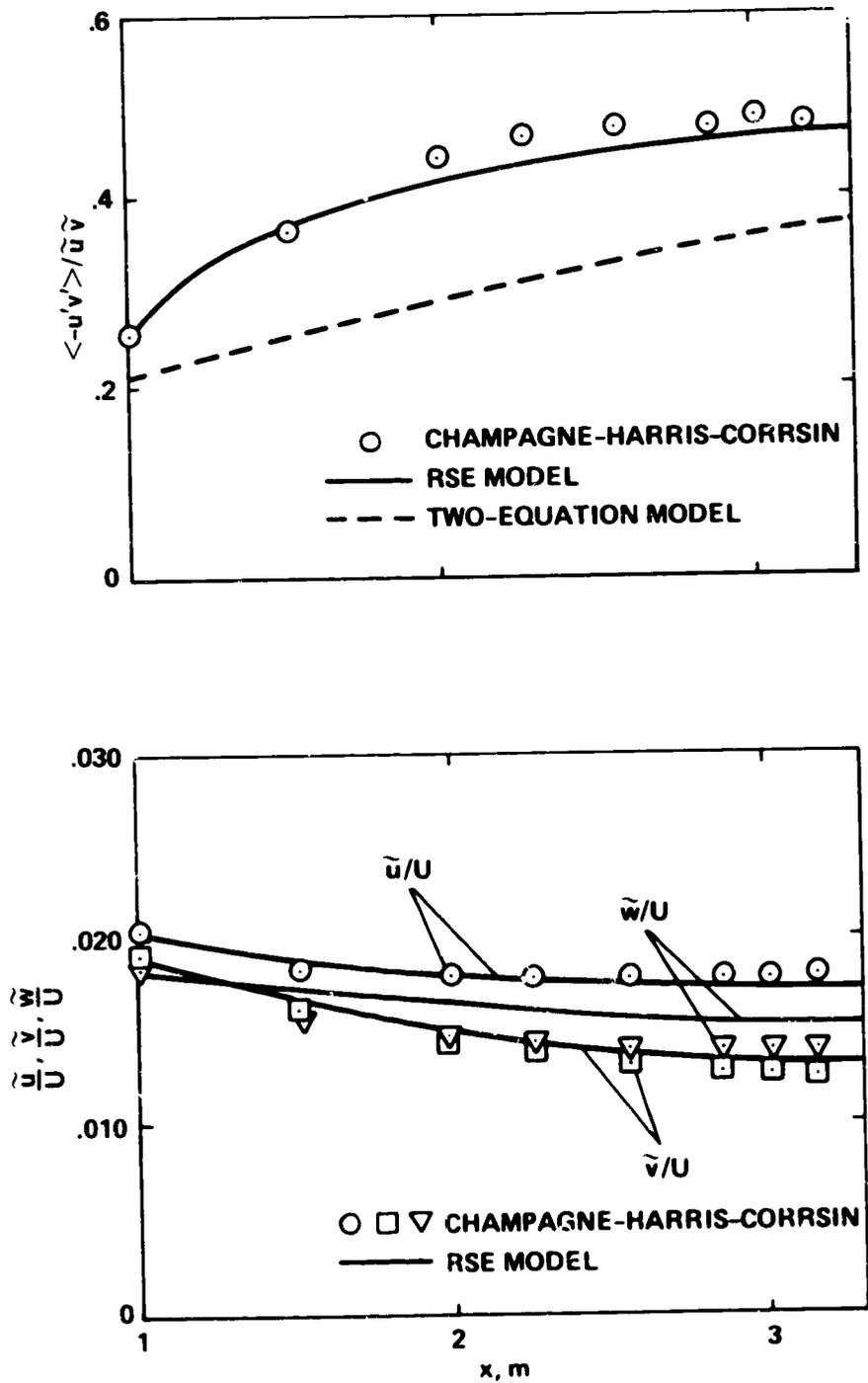
Figure 3.- Comparison of computed and measured Reynolds stresses for the
Champagne-Harris-Corrsin uniform shear flow, $\tilde{u} = \langle u'^2 \rangle^{1/2}$, $\tilde{v} = \langle v'^2 \rangle^{1/2}$,
$\tilde{w} = \langle w'^2 \rangle^{1/2}$.
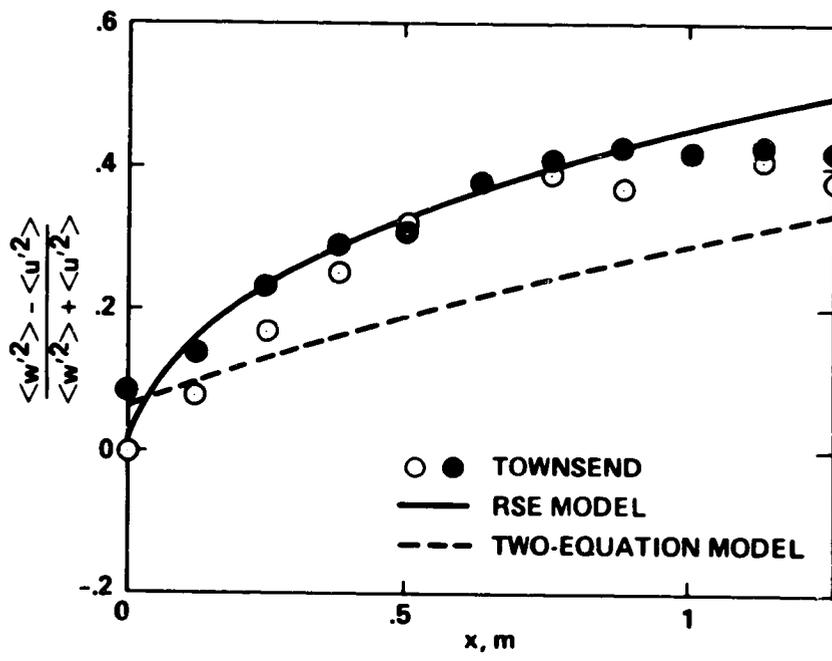
Figure 4.- Comparison of computed and measured distortion parameter for the Townsend plane strain flow.

38
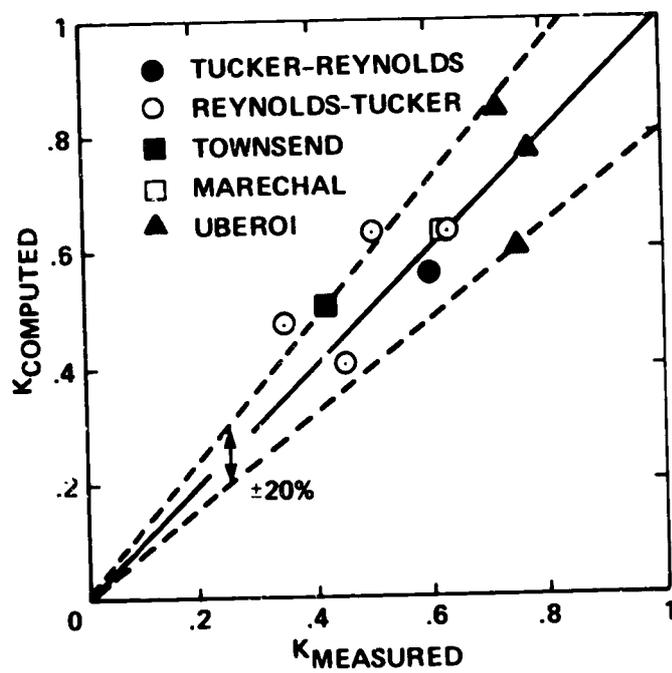
Figure 5.- Summary of RSE model computed distortion parameter for flows with plane strain.
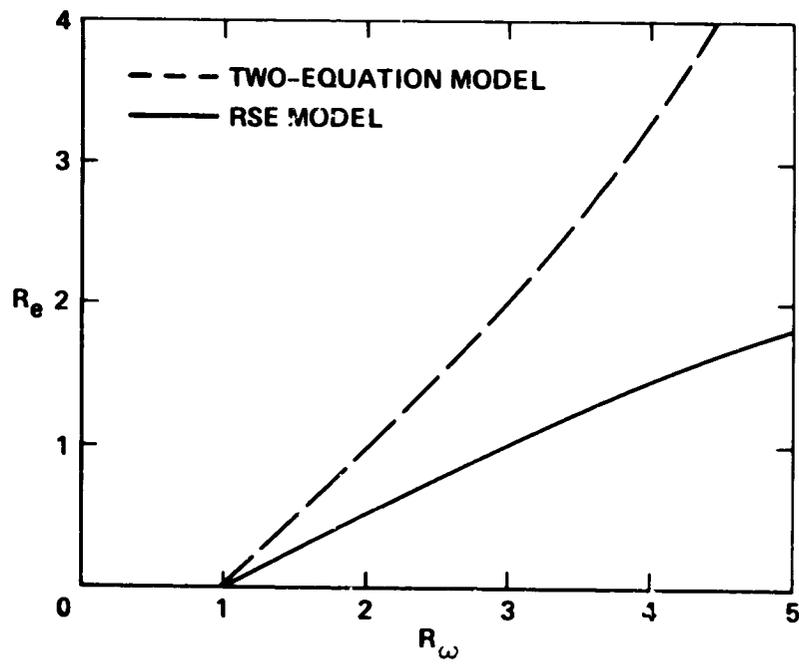
Figure 6.- Locus of values of R_e and R_ω which yield a smooth-wall constant in the law of the wall of 5.5.

40
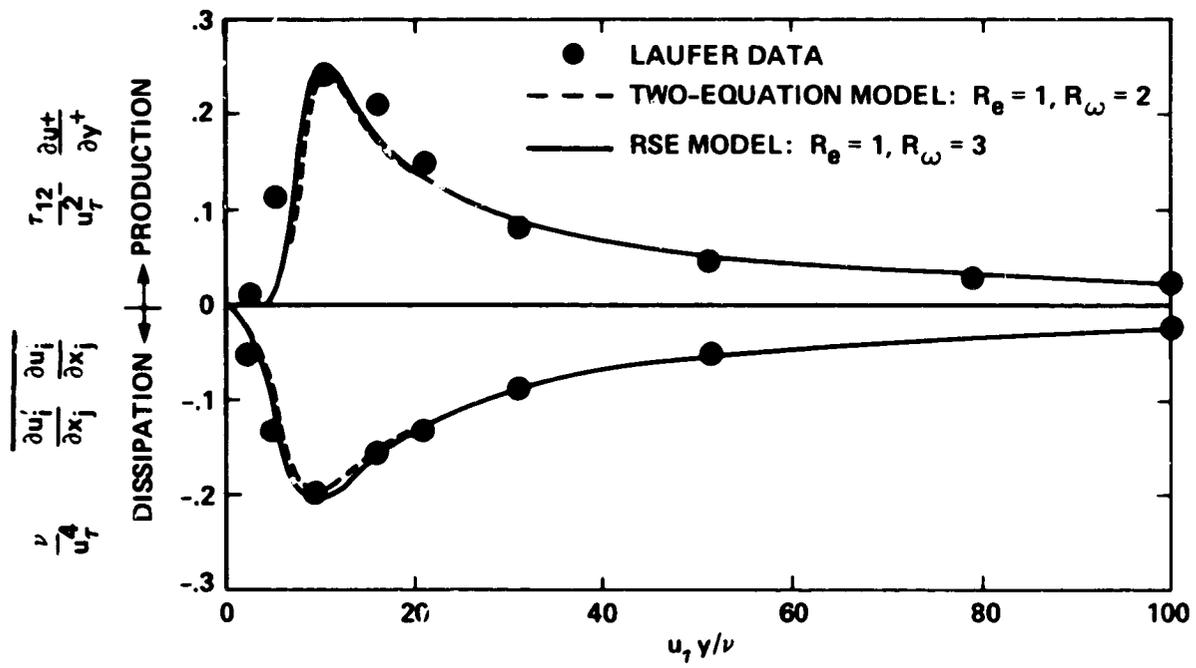
Figure 7.- Turbulence energy balance in the sublayer.

41
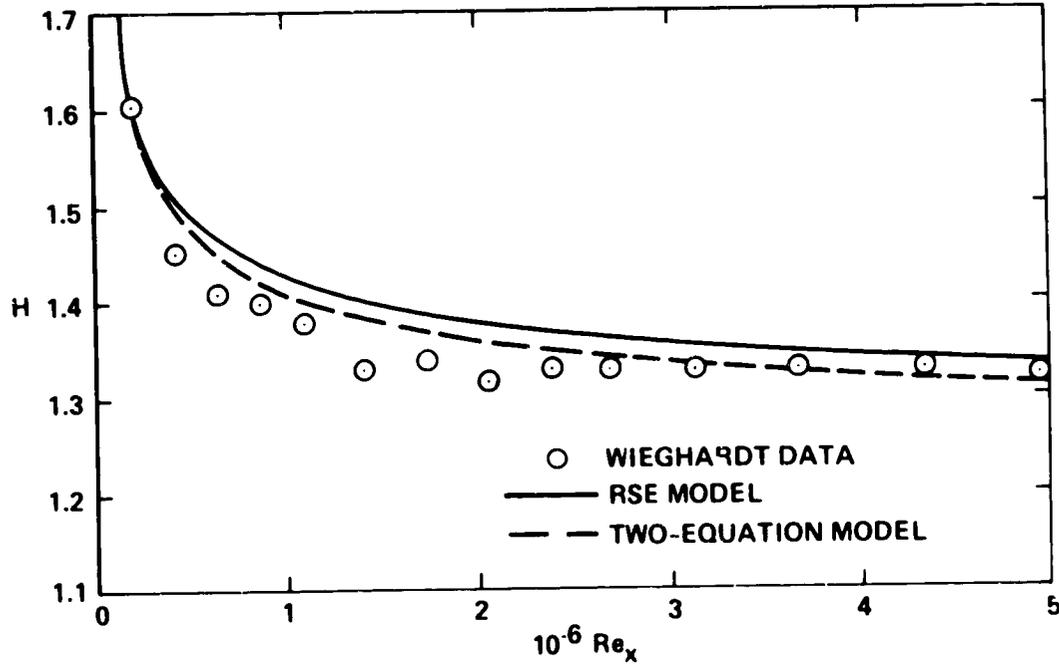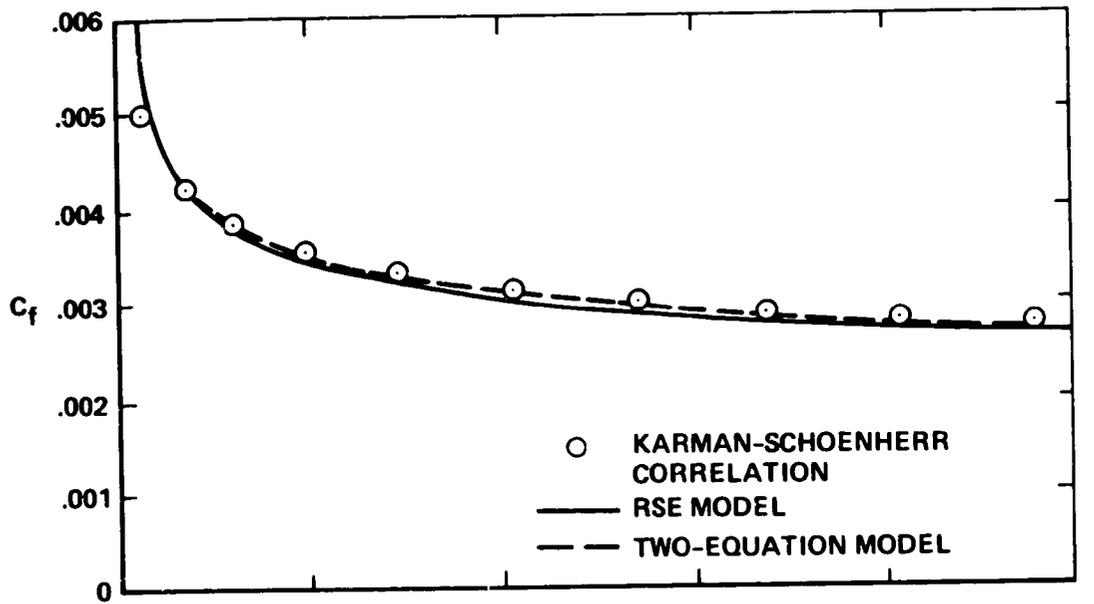
Figure 8.— Comparison of computed and measured skin friction and shape factor for flat-plate boundary-layer flow.
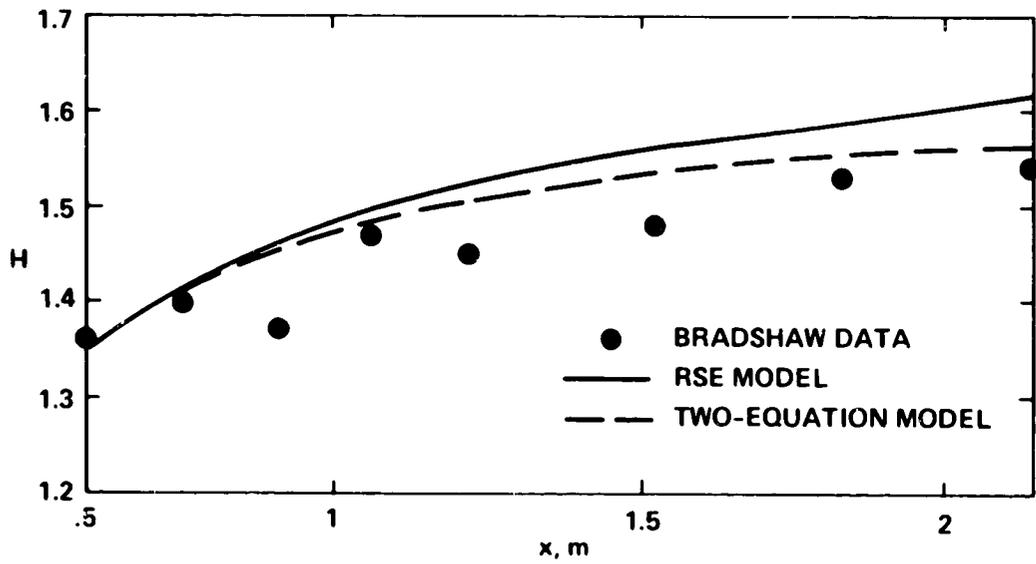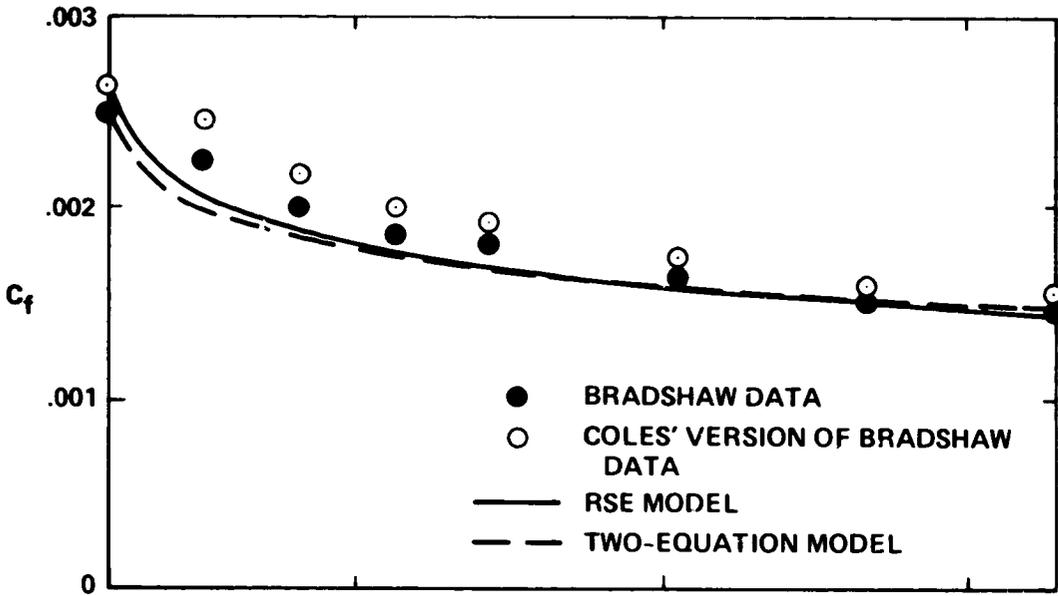
Figure 9.- Comparison of computed and measured skin friction and shape factor
for the Bradshaw adverse pressure-gradient flow.
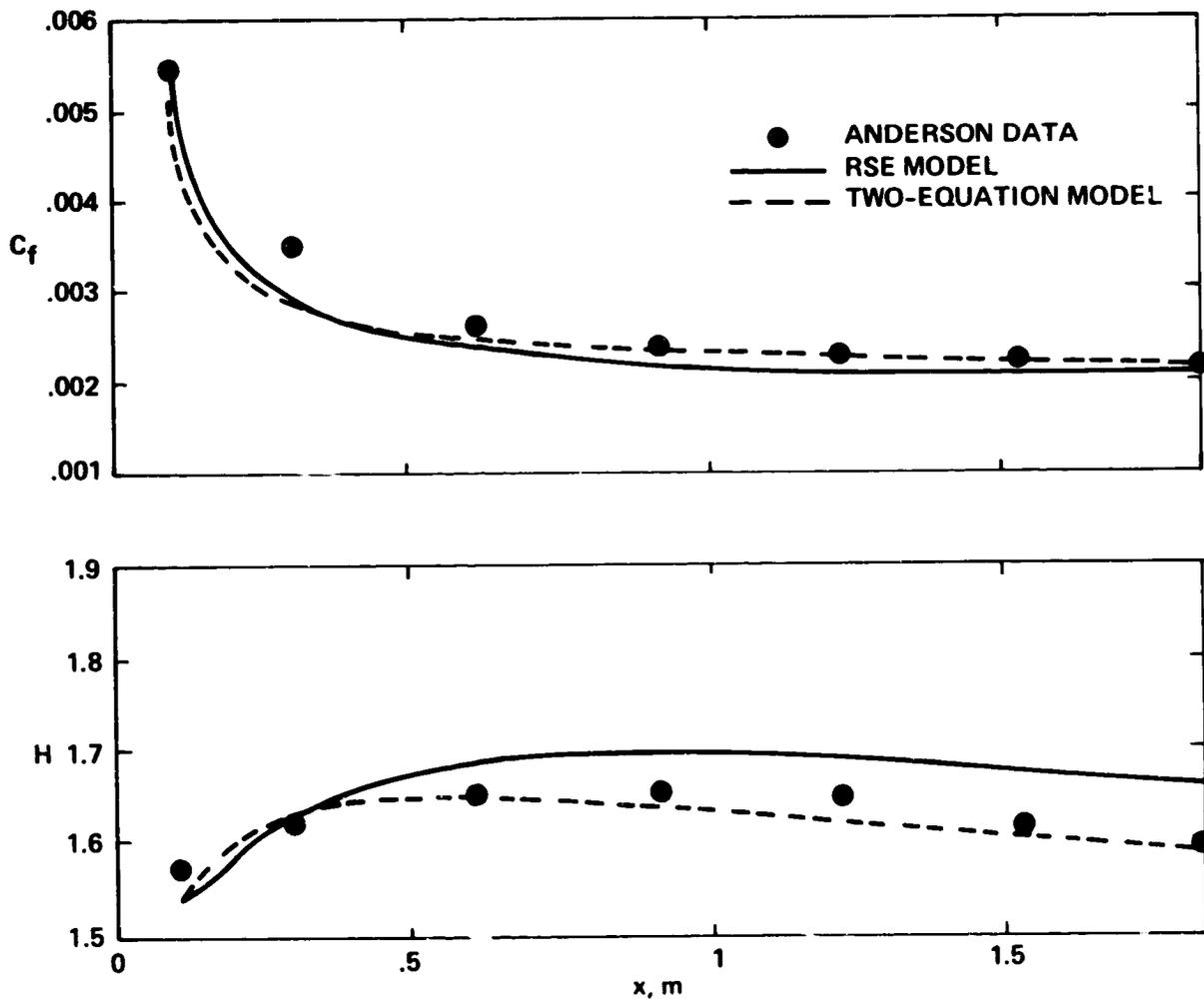
Figure 10.– Comparison of computed and measured skin friction and shape factor
for the Andersen adverse pressure-gradient flow.
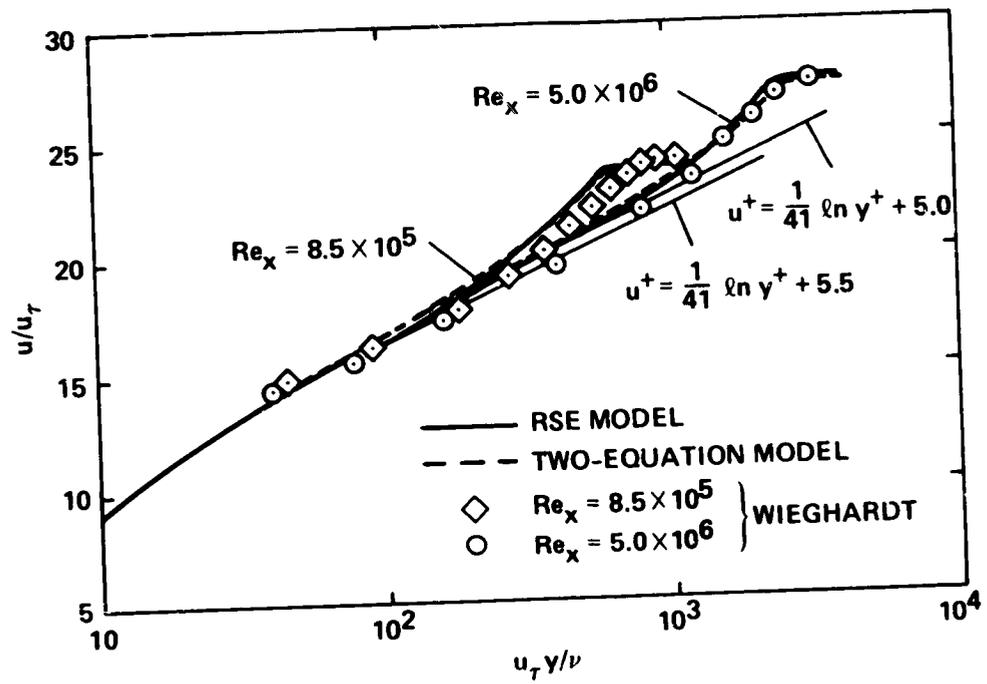
Figure 11.- Comparison of computed and measured velocity profiles for flat-plate boundary-layer flow.
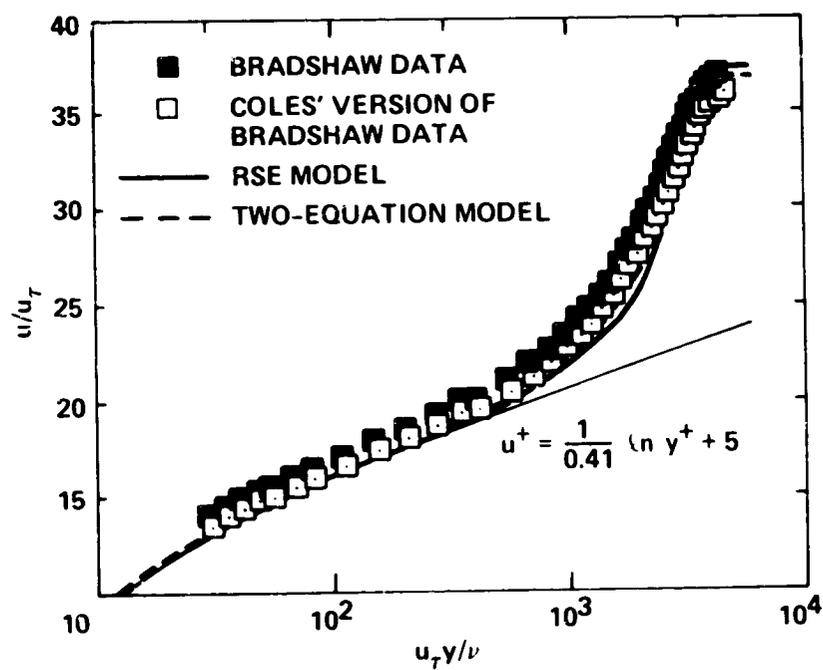
Figure 12.- Comparison of computed and measured velocity profiles for the Bradshaw adverse pressure-gradient flow, x = 2.1 m.
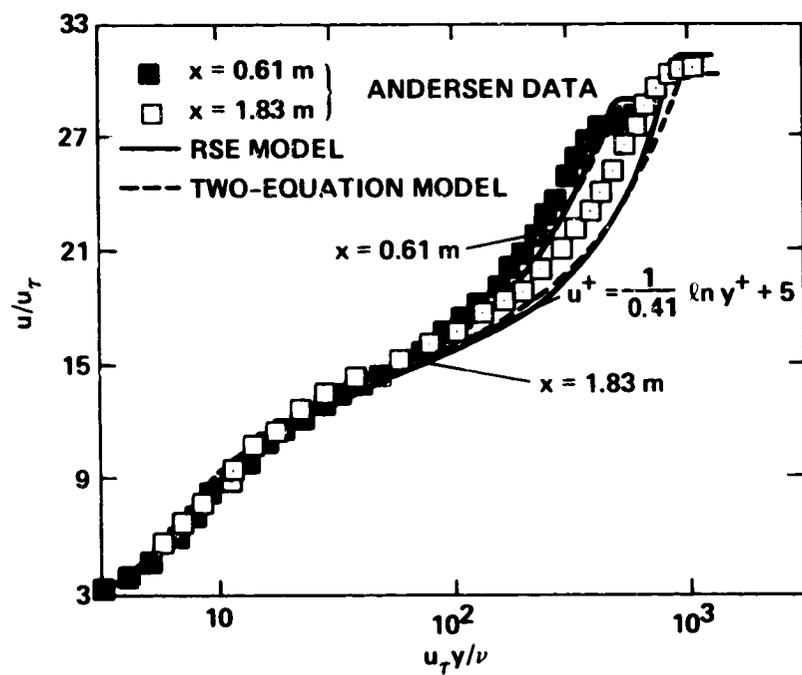
Figure 13.- Comparison of computed and measured velocity profiles for the Andersen adverse pressure-gradient flow.
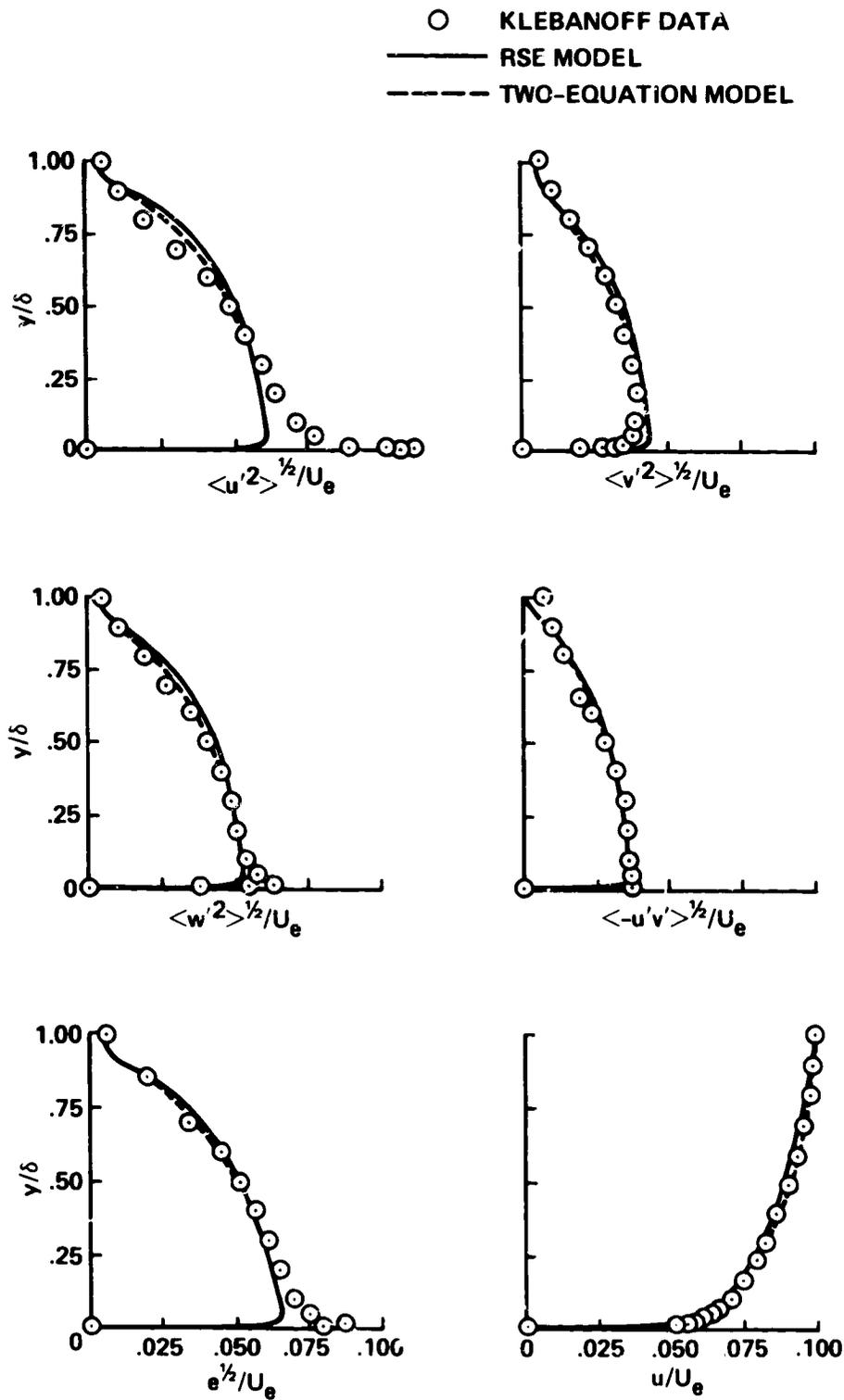
Figure 14.- Reynolds stress profiles for flat-plate boundary-layer flow, $Re_x = 4.2 \times 10^6$.

48
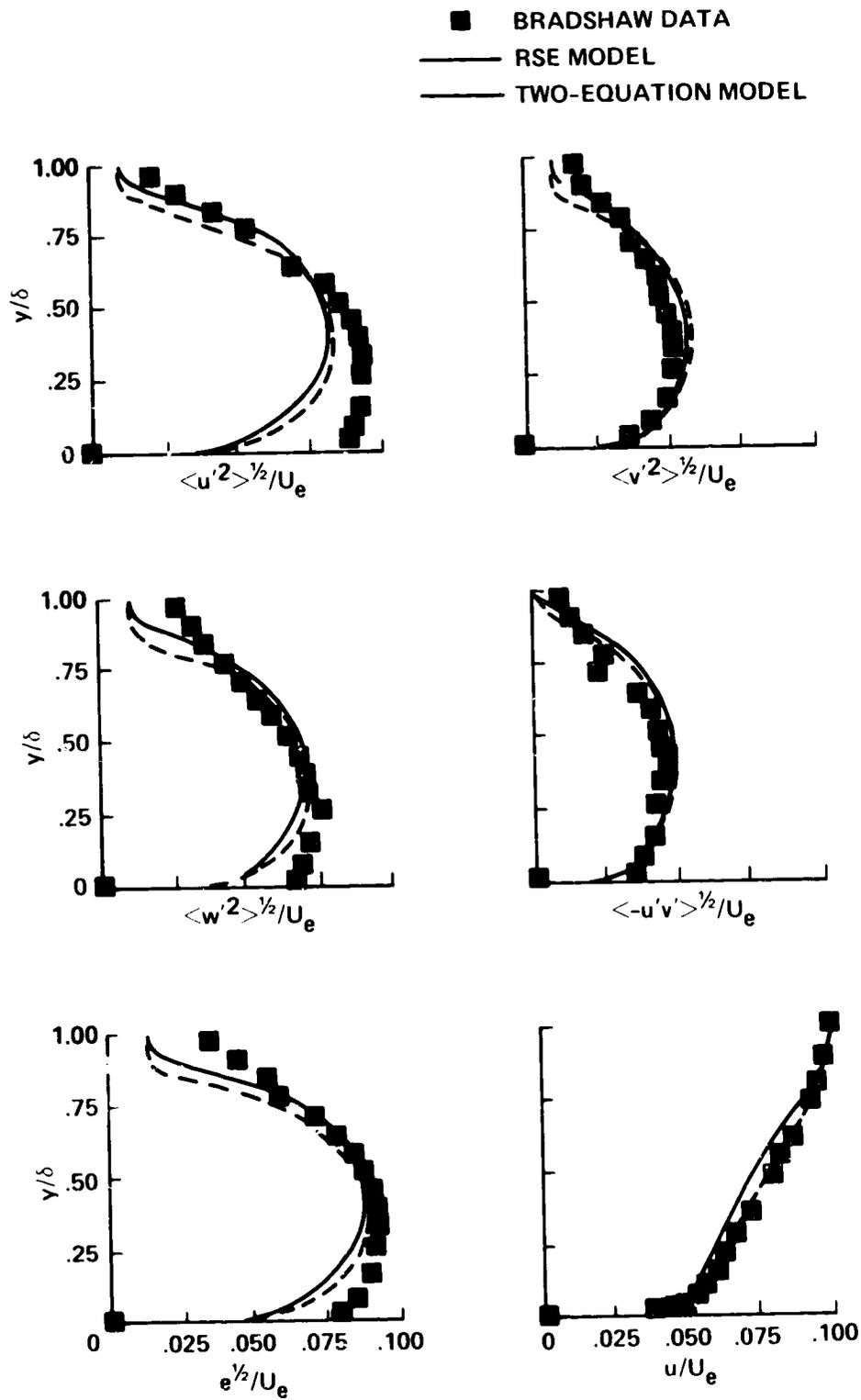
Figure 15.- Reynolds stress profiles for the Bradshaw adverse pressure-gradient flow, x = 2.1 m.

49
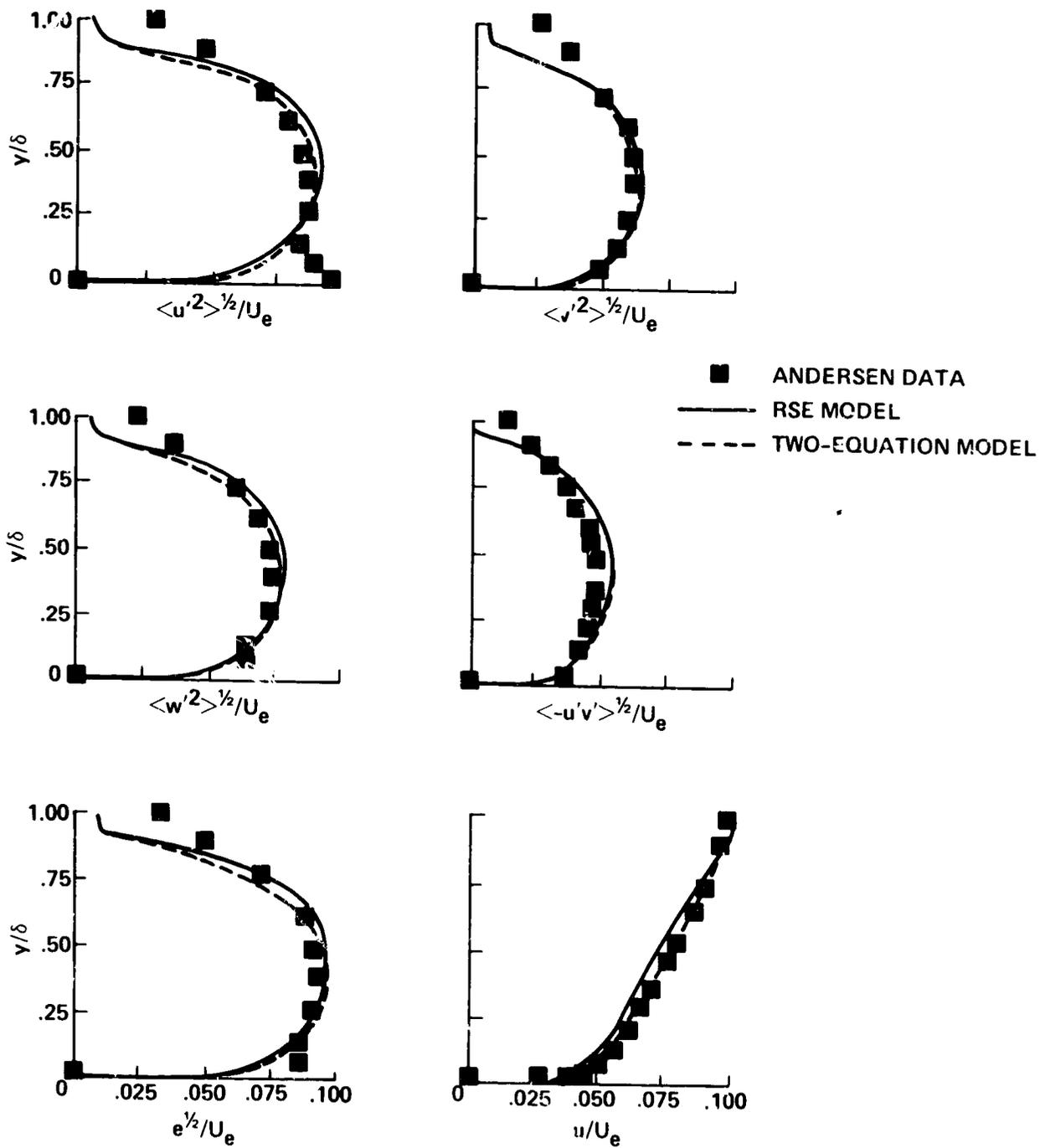
Figure 16.- Reynolds stress profiles for the Andersen adverse pressure-gradient flow, x = 1.83 m.
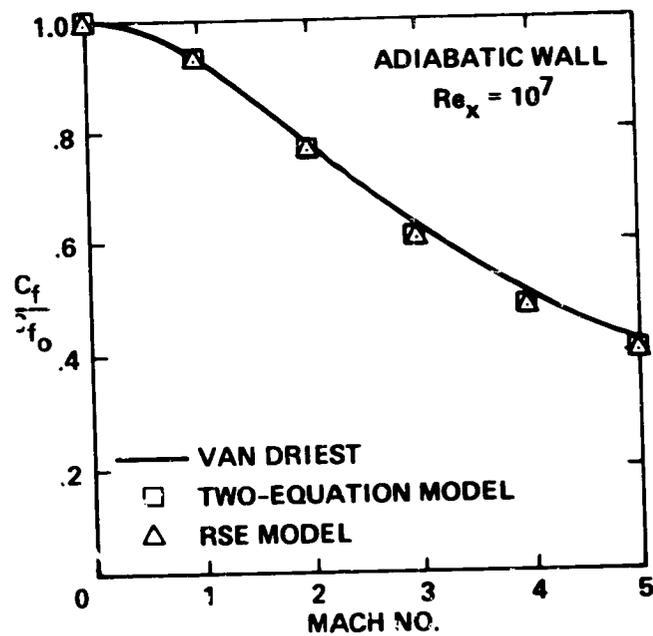
Figure 17.- Effect of compressibility on the skin friction of an insulated flat plate, $Re_x = 10^7$.
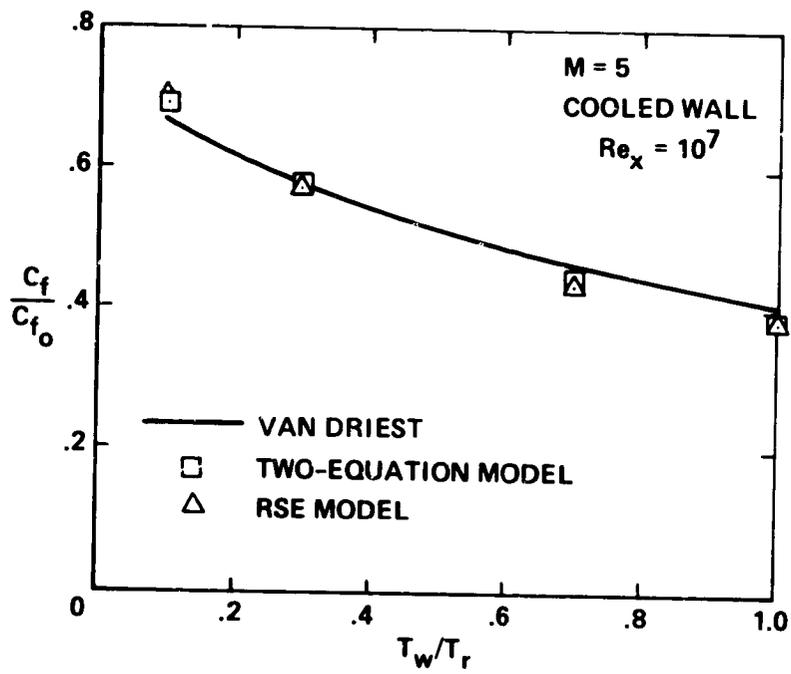
Figure 18.- Effect of surface cooling on the skin friction on a flat plate at $M = 5$, $Re_x = 10^7$.
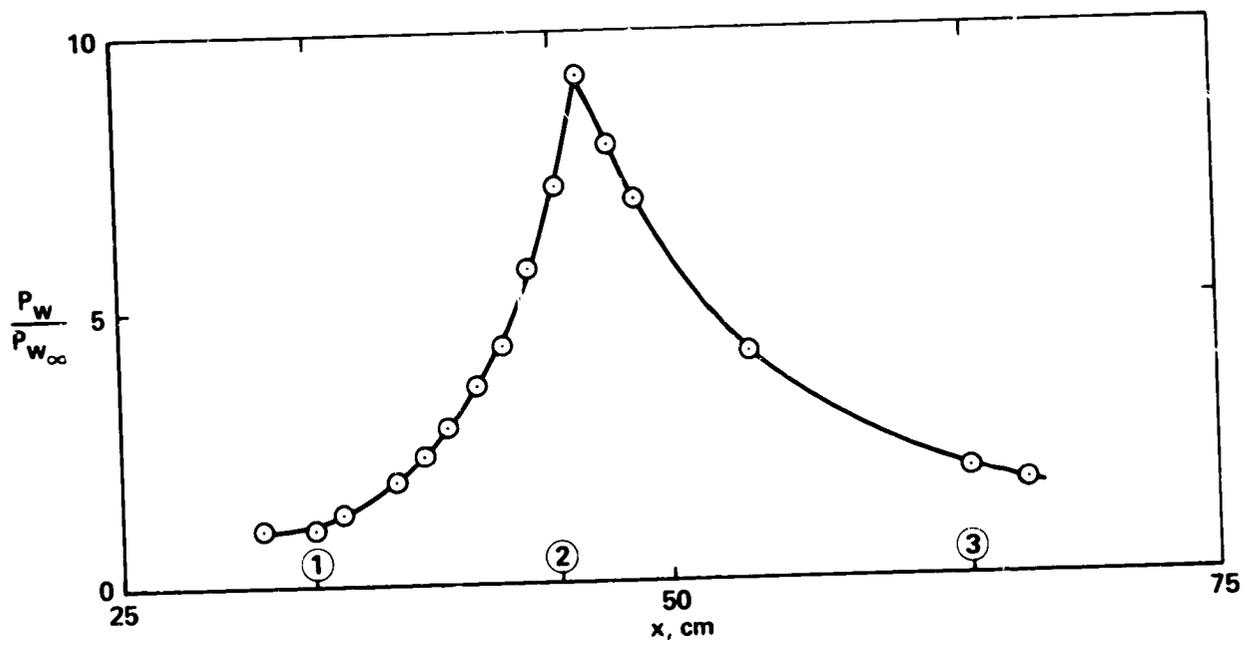
Figure 19.- Surface pressure distribution in the experiment by Lewis, Gran, and Kubota.
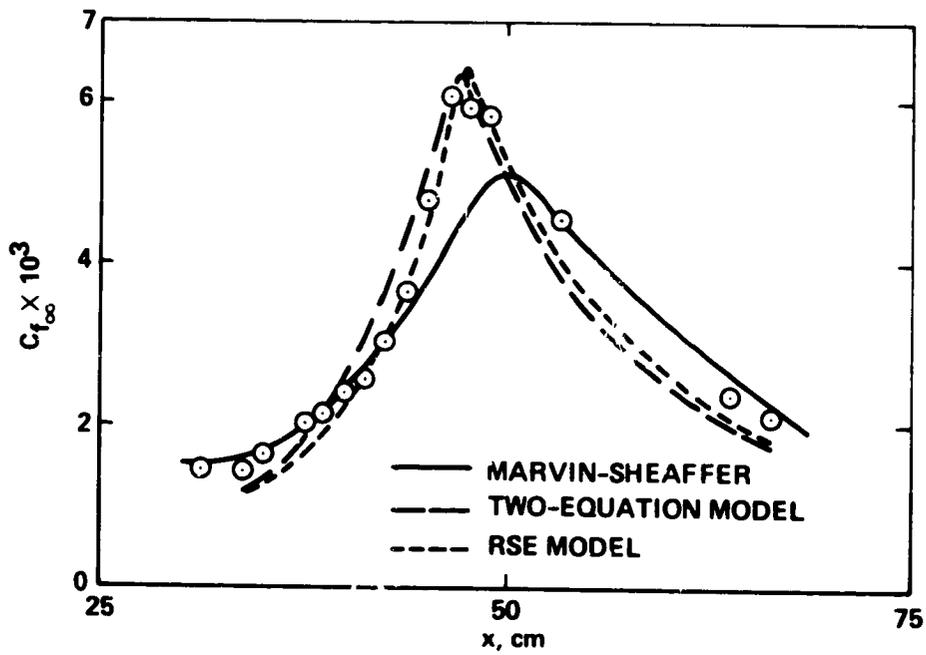
Figure 20.- Skin-friction coefficient distribution in experiment of Lewis, Gran, and Kubota.
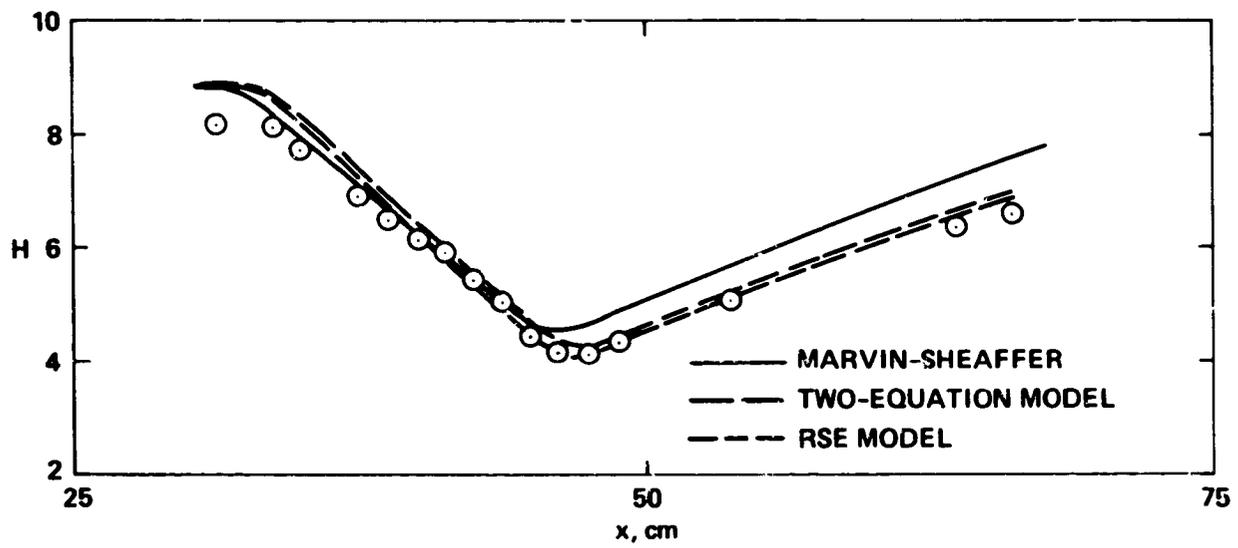
Figure 21.- Shape factor distribution in the experiment of Lewis, Gran, and Kubota.
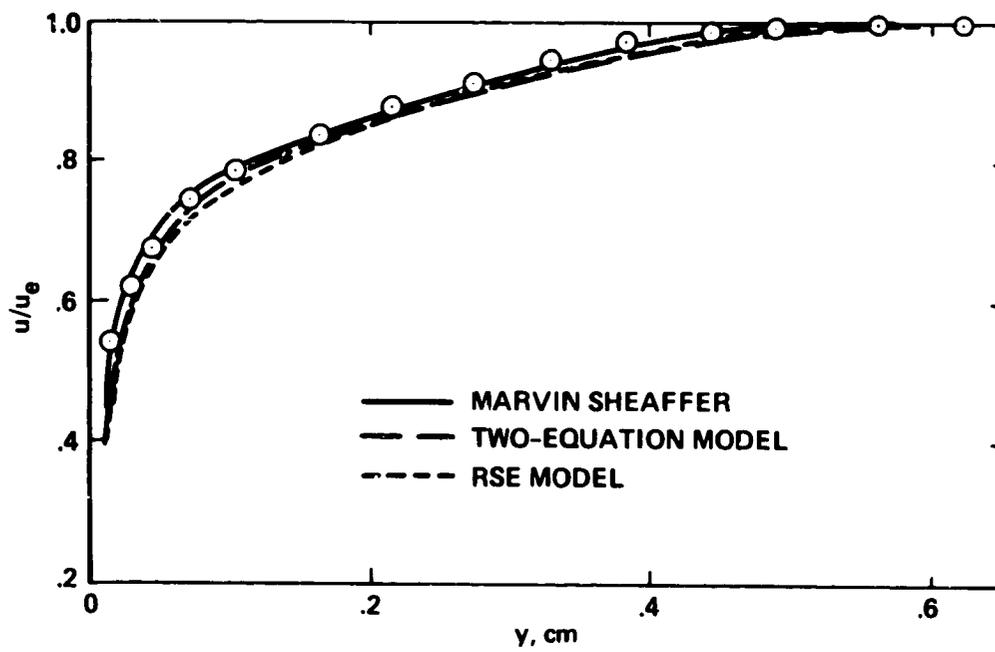
Figure 22.- Velocity profile at station 1 in experiment of Lewis, Gran, and Kubota.

56
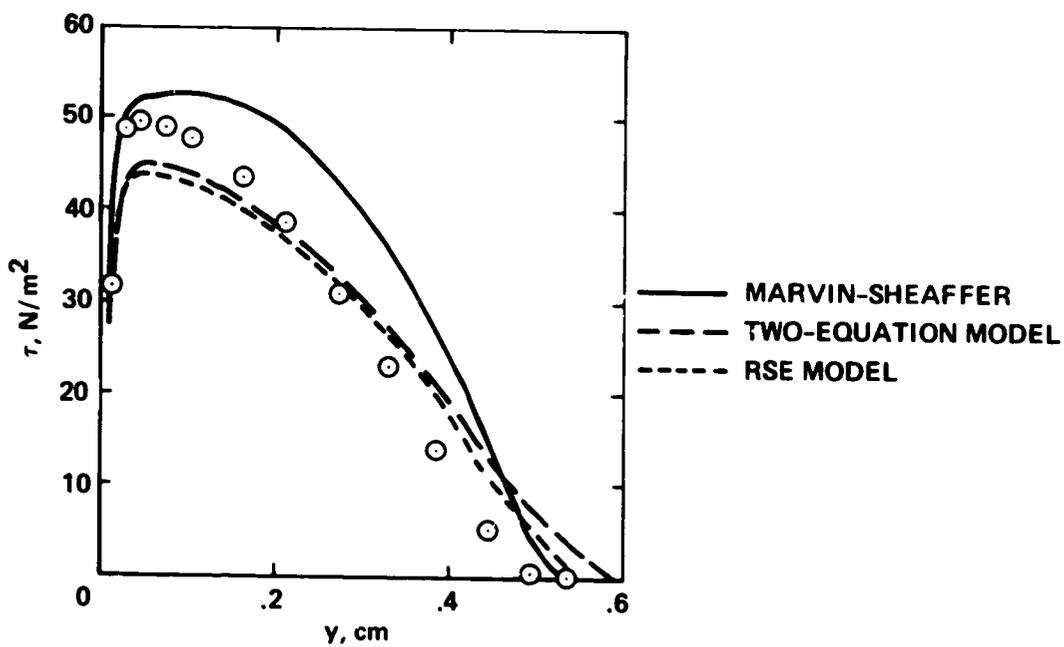
Figure 23.- Turbulent shear stress profile at station 1 in experiment by Lewis, Gran, and Kubota.
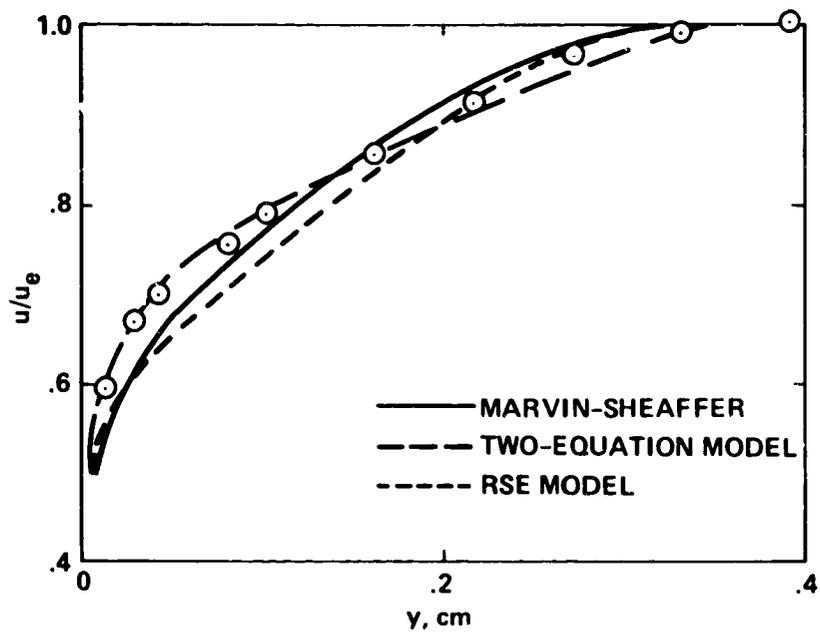
Figure 24.- Velocity profile at station 2 in experiment by Lewis, Gran, and Kubota.

58
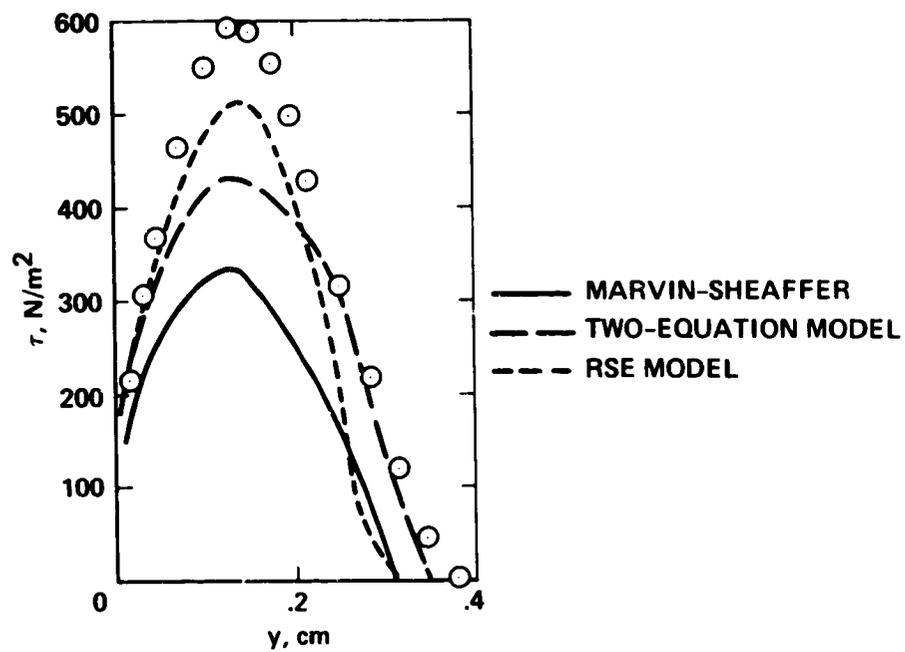
Figure 25.- Turbulent shear stress profile at station 2 in experiment by
Lewis, Gran, and Kubota.
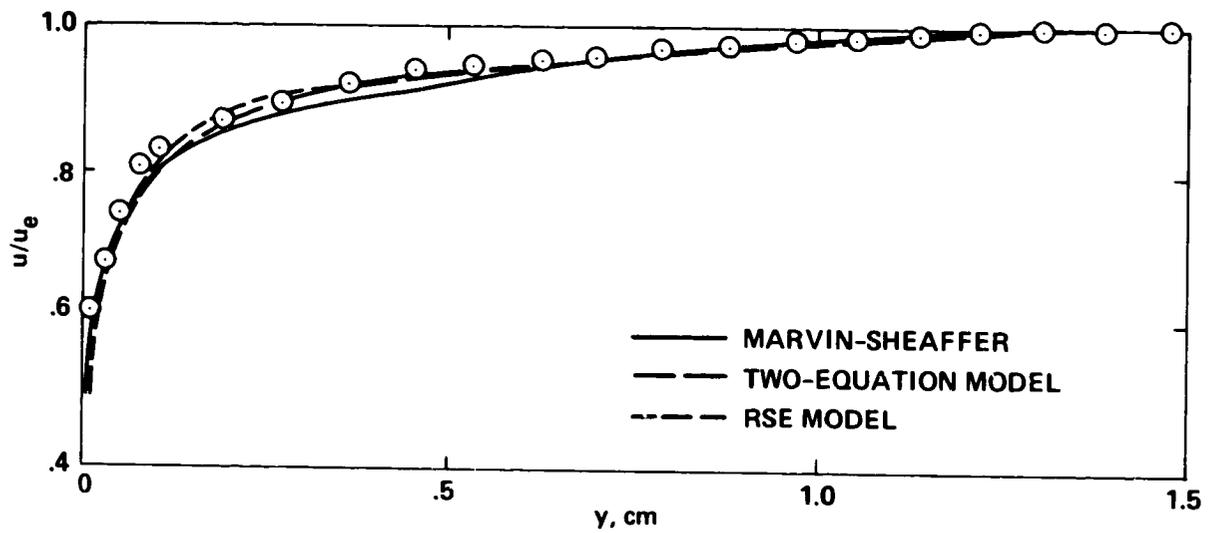
Figure 26.– Velocity profile at station 3 in experiment by Lewis, Gran, and Kubota.

60
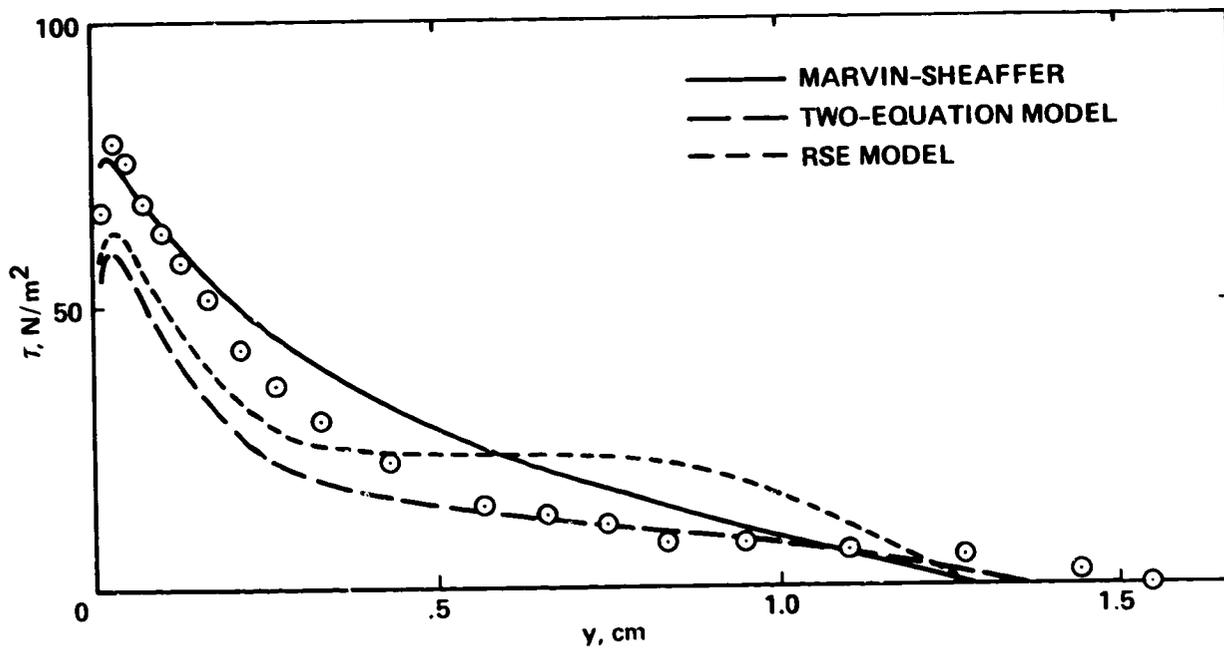
Figure 27.- Turbulent shear stress profile at station 3 in experiment by Lewis, Gran, and Kubota.
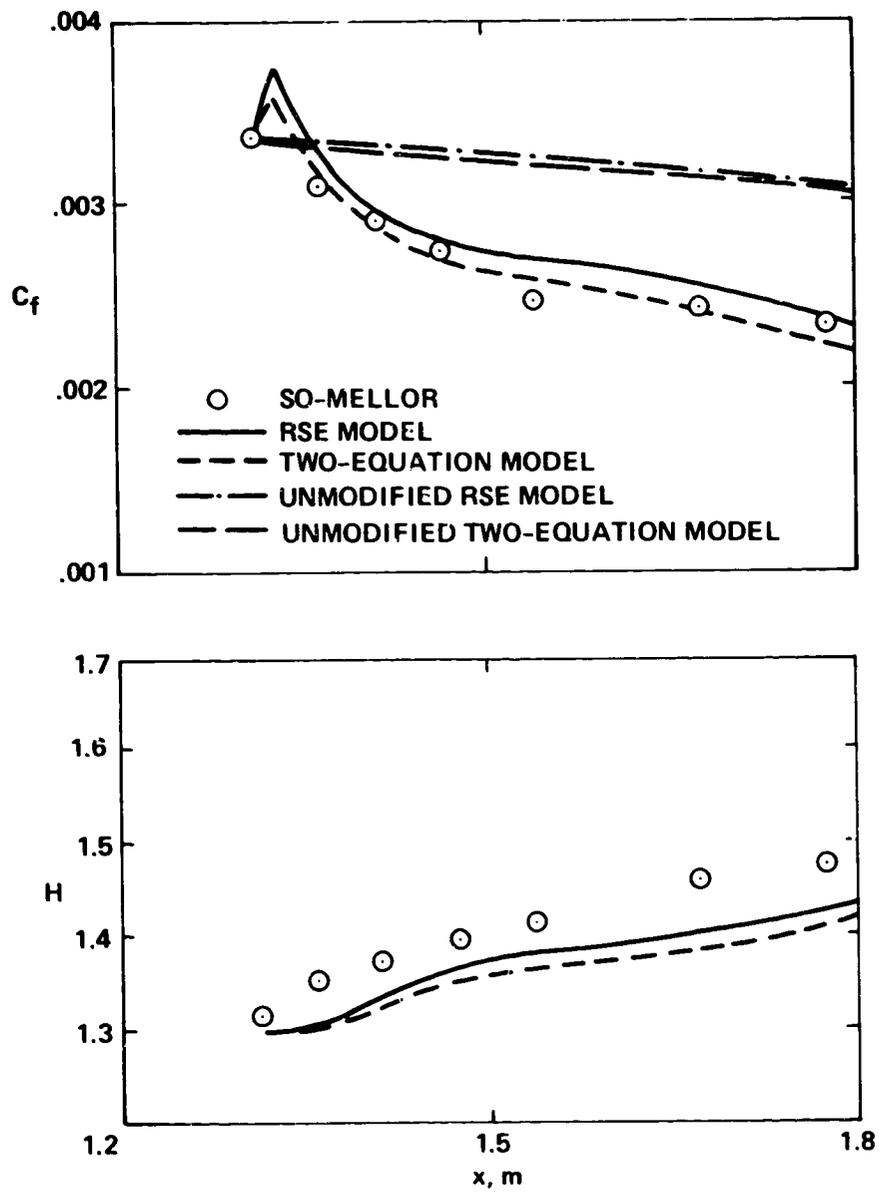
Figure 28.- Comparison of computed and measured skin friction and shape factor for flow over a convex wall with constant pressure.
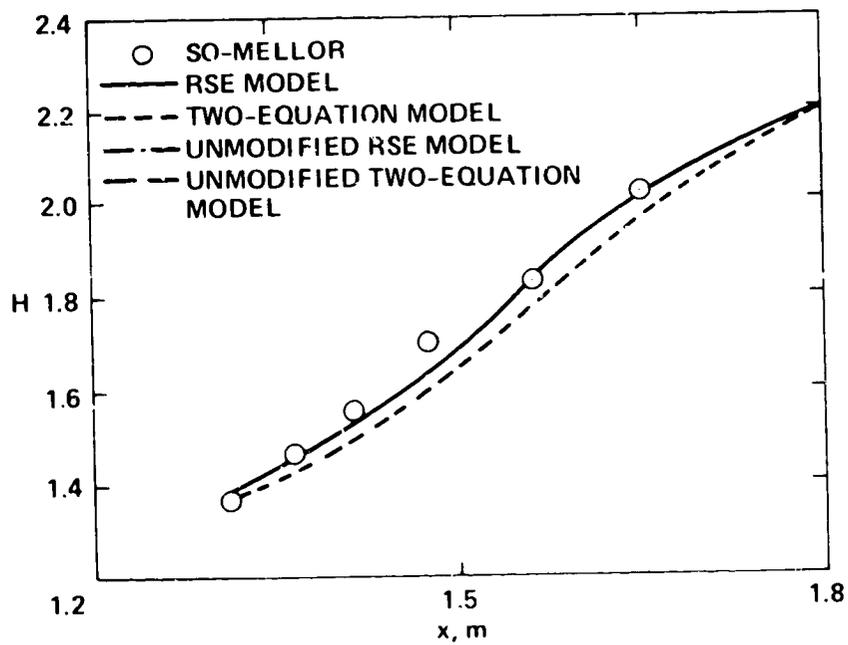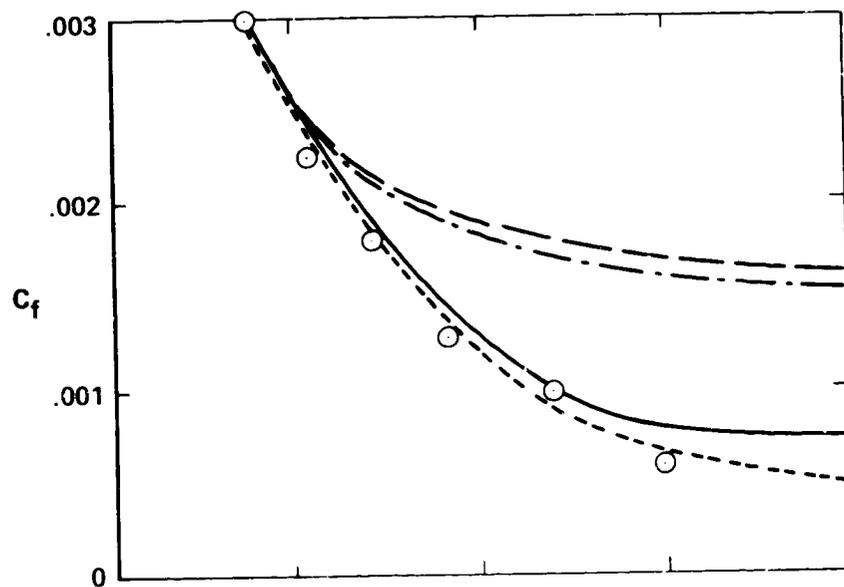
Figure 29.- Comparison of computed and measured skin friction and shape factor for flow over a convex wall with adverse pressure gradient.
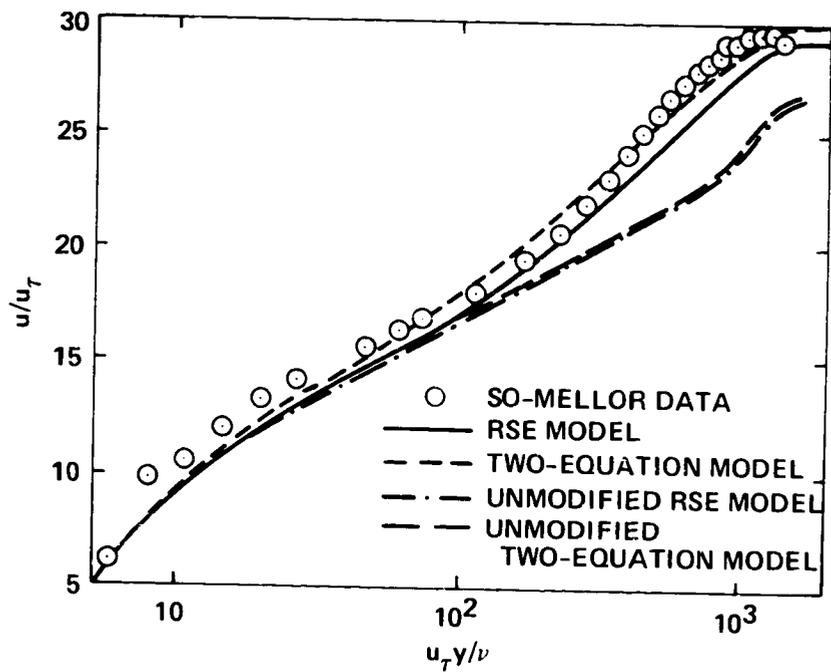
Figure 3C.- Comparison of computed and measured velocity profiles for flow over a convex wall with zero pressure gradient, x = 1.8 m.
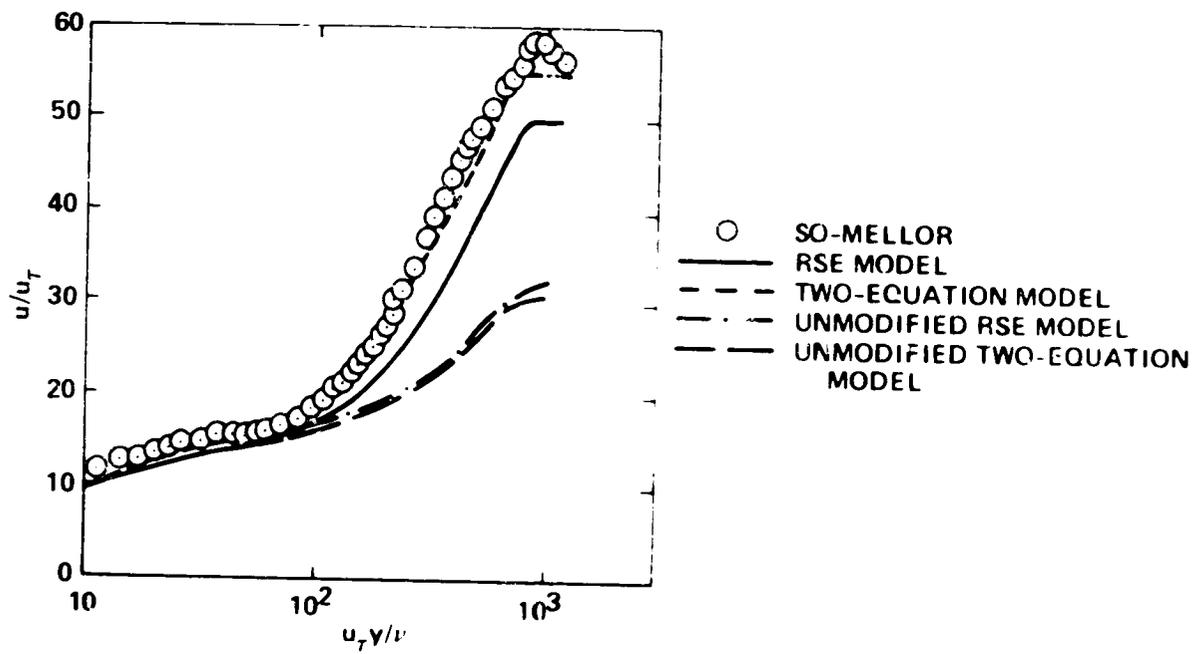
Figure 31.- Comparison of computed and measured velocity profiles for flow over a convex wall with adverse pressure gradient, x = 12.0 ft.
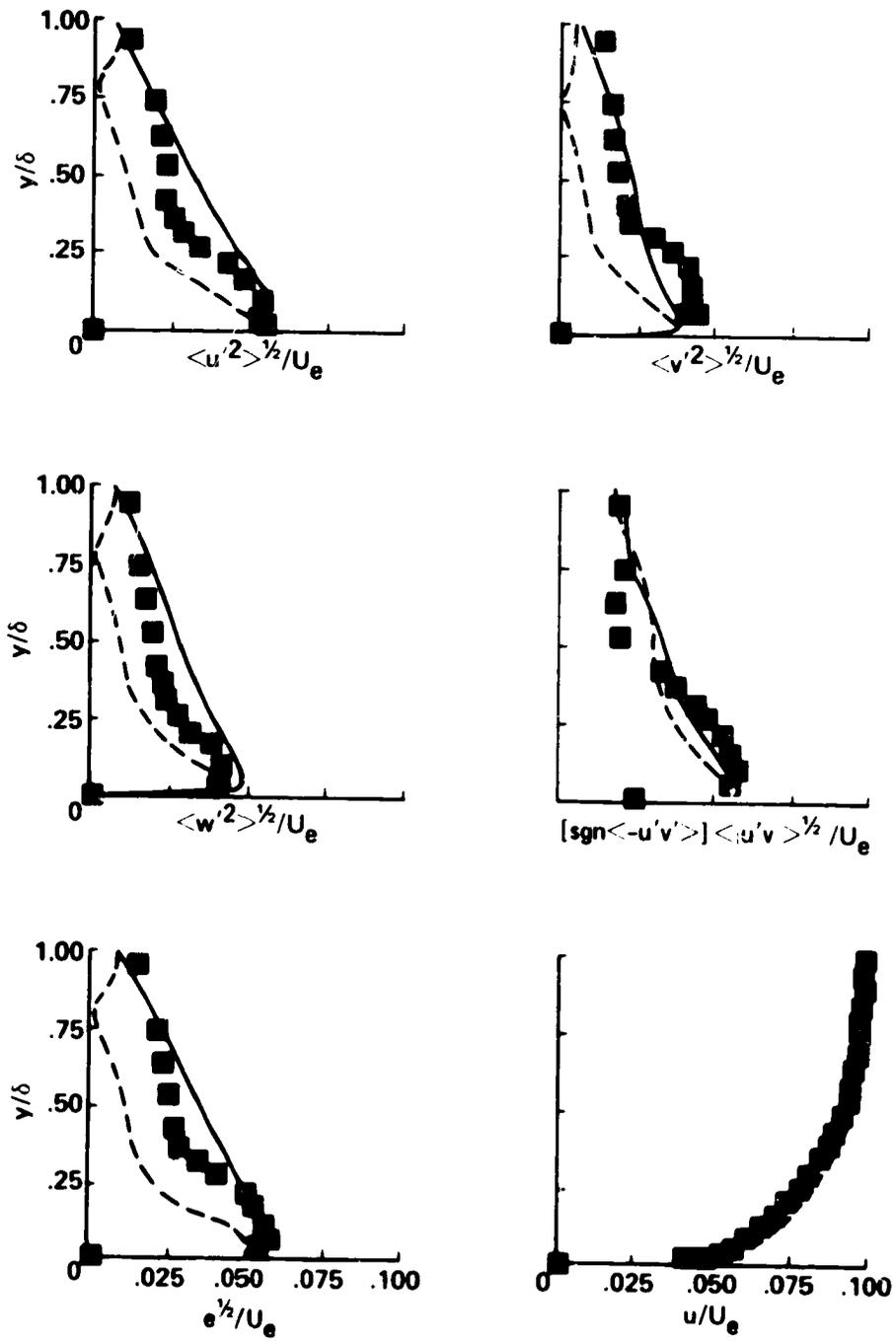
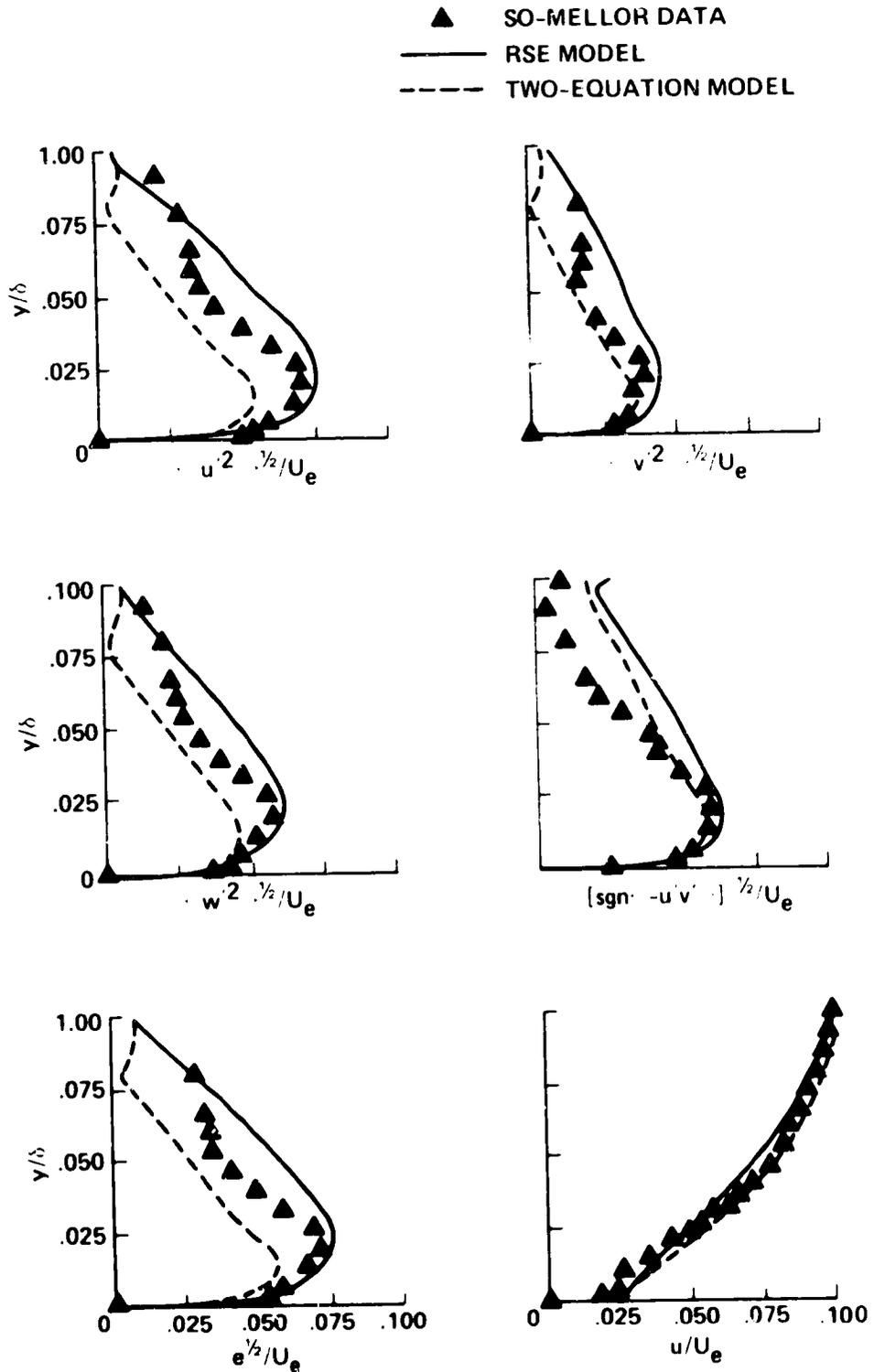Figure 32.- Reynolds stress profiles for flow over a convex surface with constant pressure, x = 1.5 m.

Figure 33.- Reynolds stress profiles for flow over a convex surface with adverse pressure gradient, x = 1.7 m.

67